

OPTIMIZATION OF WELL CONFIGURATION
FOR A SEDIMENTARY ENHANCED
GEOHERMAL RESERVOIR

by
Mengnan Zhou

A thesis submitted to the Faculty and the Board of Trustees of the Colorado School of Mines in partial fulfillment of the requirements for the degree of Master of Science (Petroleum Engineering).

Golden, Colorado

Date _____

Signed: _____
Mengnan Zhou

Signed: _____
Dr. Luis E. Zerpa
Thesis Advisor

Golden, Colorado

Date _____

Signed: _____
Dr. Erdal Ozkan
Professor and Head
Department of Petroleum Engineering

ABSTRACT

The extraction of geothermal energy in the form of hot water from sedimentary rock formations could expand the current geothermal energy resources toward new regions. In sedimentary geothermal reservoirs with low permeability, enhancement techniques (e.g., well hydraulic stimulation) are needed to improve the hydraulic connection between the wells to achieve commercial production/injection rates (Cho et al. 2015). The design of the well configuration was investigated in this research work. The performance of the sedimentary geothermal reservoir was evaluated using numerical reservoir modeling, which allowed studying different well configurations and productivity enhancement techniques. This research develops a methodology to maximize thermal recovery from the geothermal system. The objective is to maximize the well productivity/injectivity index by systematically changing the value of influencing variables of the system, subject to a constraint of thermal breakthrough time greater than or equal to 30 years (i.e., time required by a commercial successful project).

The reservoir simulation cases are classified into four main models based on well configuration, shown in Figure 3.3: one vertical well doublet system with hydraulic fractures, and three horizontal well configurations with open-hole completion, longitudinal fractures and transverse fractures, respectively. Since permeability is the fundamental property which decides the necessity of enhancement techniques, the proper permeability estimation is selected first.

Based on that and sensitivity analysis of the variables, including well type (vertical or horizontal), well spacing, length of horizontal section, hydraulic fracture direction, fracture half-length, fracture spacing, dimensionless fracture conductivity and ratio of reservoir vertical permeability to horizontal permeability, the most efficient well configuration and the corresponding influential variables are determined. The application of this methodology provides the procedure to identify the required hydraulic fracture parameters for each well configuration that maximizes the geothermal energy recovery.

The final step is to identify the optimization of well configuration. Surface response models based on the multiple linear regression method are built to analyze the change of reservoir thermal evolution and flow behavior in terms of influential parameters in well configuration. A horizontal

well system with longitudinal fractures is most favorable in pursuing a long thermal breakthrough time. A horizontal well system with multi-stage transverse fractures is the most efficient configuration to increase the productivity index and injectivity index. For optimal well configuration designs in both well configurations, the well spacing is assigned to the minimum value, and the well horizontal length can be chosen as long as reservoir and technique permit. This design achieves minimum the thermal breakthrough time requirement and maximum productivity and injectivity indices.

TABLE OF CONTENTS

ABSTRACT iii

LIST OF FIGURES vii

LIST OF TABLES xi

NOMENCLATURE xii

ACKNOWLEDGMENTS xiv

CHAPTER 1 INTRODUCTION 1

 1.1 Motivation of Study 1

 1.2 Objective 3

 1.3 Methodology 4

CHAPTER 2 STATIC RESERVOIR MODEL 8

 2.1 Geothermal projects in the world 8

 2.2 Lyons formation 10

 2.3 Generation of static reservoir model 10

CHAPTER 3 RESERVOIR SIMULATION 15

 3.1 Preliminary cases for three permeability models 15

 3.1.1 Preliminary cases in low permeability reservoir model 20

 3.1.2 Preliminary cases in intermediate permeability reservoir model 21

 3.1.3 Preliminary cases in high permeability reservoir model 22

 3.2 Sensitivity analysis for well configuration parameters 22

 3.2.1 Model A - vertical well doublet system with hydraulic fractures 22

 3.2.2 Model B - horizontal well doublet system with open-hole completion 25

3.2.3	Model C - horizontal well doublet system with longitudinal fractures	32
3.2.4	Model D - horizontal well doublet system with transverse fractures	36
3.3	Optimization on horizontal wells with longitudinal hydraulic fractures	45
3.3.1	Surface response model for cumulative water produced volume in horizontal wells with longitudinal hydraulic fractures	47
3.3.2	Surface response model for productivity index in horizontal wells with longitudinal hydraulic fractures	49
3.3.3	Optimal well configuration in horizontal wells with longitudinal hydraulic fractures	51
3.4	Optimization on horizontal wells with multi-stage transverse fractures	54
3.4.1	Surface response model for cumulative water produced volume in horizontal wells with multi-stage transverse fractures	55
3.4.2	Surface response model for productivity index in horizontal wells with multi-stage transverse fractures	57
3.4.3	Optimal well configuration in horizontal wells with multi-stage transverse fractures	58
3.5	Summary	60
CHAPTER 4 CONCLUSIONS AND SUGGESTIONS		61
4.1	Conclusions	61
4.2	Suggestions	62
REFERENCES CITED		63
APPENDIX A - RESERVOIR PROPERTIES		66
APPENDIX B - SIMULATION PROPERTIES CALCULATION		68
APPENDIX C - CORE MEASUREMENTS DATA		70

LIST OF FIGURES

Figure 2.1	Electric Generation Capacity by Fuel Type in California, modified from	9
Figure 2.2	Location of Denver Basin, with Wattenberg field highlighted	11
Figure 2.3	Stratigraphic Section of Rock Units in Outcrop and the Adjacent Denver Basin .	12
Figure 2.4	Temperature distribution for candidate area.	14
Figure 2.5	Porosity distribution for candidate area.	14
Figure 3.1	Permeability-Porosity correlation for different core samples.	17
Figure 3.2	Vertical well doublet system (one injection well and one production well). . . .	18
Figure 3.3	Models A, B, C and D with different well configurations.	18
Figure 3.4	Summary of thermal breakthrough and change of production well flowrate as time changes for preliminary cases in low permeability reservoir model.	20
Figure 3.5	Summary of thermal breakthrough and change of production well flowrate as time changes for preliminary cases in intermediate permeability reservoir model.	21
Figure 3.6	Summary of thermal breakthrough and change of production well flowrate as time changes for preliminary cases in high permeability reservoir model.	22
Figure 3.7	Model A (vertical well doublet system with hydraulic fractures).	23
Figure 3.8	Summary of thermal breakthrough time and change of productivity index in the process of time for vertical wells with fractures cases with different well spacing values.	24
Figure 3.9	Summary of thermal breakthrough time and change of productivity index in the process of time for vertical well with fractures cases with different fracture half-length values.	25
Figure 3.10	Aerial view temperature distribution after 5 years of production for vertical wells with fractures, with fracture half-lengths of 250 m (a), 500 m (b) and 750 m (c), and aerial view permeability distribution for vertical wells with fractures, with fracture half-length of 750 m (d).	26
Figure 3.11	Summary of thermal breakthrough time and change of productivity index in the process of time for vertical well with fractures cases with different dimensionless fracture conductivity values.	27

Figure 3.12	Production flow rate as function of time for vertical well with fractures cases with different dimensionless fracture conductivity values.	27
Figure 3.13	Summary of thermal breakthrough time and change of productivity index in the process of time for vertical well with fractures cases with different ratio of reservoir vertical permeability to horizontal permeability values.	28
Figure 3.14	Model B (horizontal well doublet system with open-hole completion).	29
Figure 3.15	Summary of thermal breakthrough time and change of productivity index in the process of time for horizontal wells with open-hole completion cases with different well spacing values.	29
Figure 3.16	Summary of thermal breakthrough time and change of productivity index in the process of time for horizontal wells with open-hole completion cases with different horizontal section length values.	30
Figure 3.17	Aerial view temperature distribution after 30 years of production for horizontal wells with open-hole completion, with horizontal section lengths 1.0 km (a), 1.5 km (b), and 2.0 km (c).	31
Figure 3.18	Summary of thermal breakthrough time and change of productivity index in the process of time for horizontal well with open-hole completion cases with different ratio of reservoir vertical permeability to horizontal permeability values.	32
Figure 3.19	Zoomed lateral view temperature distribution after 3 years of production for horizontal wells with open-hole completion, with ratio of reservoir vertical permeability to horizontal permeability values of 0.01 (a), 0.1 (b), and 1 (c).	33
Figure 3.20	Model C (horizontal well doublet system with longitudinal fractures).	34
Figure 3.21	Summary of thermal breakthrough time and change of productivity index in the process of time for horizontal well with longitudinal fractures cases with different well spacing values.	35
Figure 3.22	Summary of thermal breakthrough time and change of productivity index in the process of time for horizontal well with longitudinal fractures cases with different horizontal section length values.	35
Figure 3.23	Summary of thermal breakthrough time and change of productivity index in the process of time for horizontal well with longitudinal fractures cases with different dimensionless fracture conductivity values.	36
Figure 3.24	Aerial view temperature distribution after 1 year of production for horizontal well with longitudinal fractures cases with dimensionless fracture conductivity values of 0.01 (a), 0.1 (b) and 1 (c).	37

Figure 3.25	Summary of thermal breakthrough time and change of productivity index in the process of time for horizontal well with longitudinal fractures cases with different ratio of reservoir vertical permeability to horizontal permeability values.	38
Figure 3.26	Model D (horizontal well doublet system with transverse fractures).	38
Figure 3.27	Summary of thermal breakthrough time and change of productivity index in the process of time for horizontal well with transverse fracture cases with different well spacing values.	39
Figure 3.28	Summary of thermal breakthrough time and change of productivity index in the process of time for horizontal well with transverse fracture cases with different fracture half-length values.	39
Figure 3.29	Summary of thermal breakthrough time and change of productivity index in the process of time for horizontal well with transverse fracture cases with different horizontal section length values.	41
Figure 3.30	Summary of thermal breakthrough time and change of productivity index in the process of time for horizontal well with transverse fracture cases with different fracture spacing values.	41
Figure 3.31	Change of production well flow rate as time changes for horizontal well with transverse fracture cases with different fracture spacing values.	42
Figure 3.32	Summary of thermal breakthrough time and change of productivity index in the process of time for horizontal well with transverse fracture cases with different dimensionless fracture conductivity values.	42
Figure 3.33	Aerial view temperature distribution after 1 year of production for horizontal well with transverse fracture cases with different dimensionless fracture conductivity values of 1.0 (a), 1.5 (b) and 10.0 (c).	43
Figure 3.34	Summary of thermal breakthrough time and change of productivity index in the process of time for horizontal well with transverse fracture cases with different ratio of reservoir vertical permeability to horizontal permeability values.	44
Figure 3.35	Summary of thermal breakthrough and change of productivity index in the process of time horizontal well with transverse fracture cases with same fracture surface area.	45
Figure 3.36	Flow vector distribution of horizontal wells with longitudinal fractures after one year of production. Full view on the left and zoomed in view on the right. .	48

Figure 3.37	3D plot of cumulative water produced volume as function of horizontal section length and well spacing in horizontal wells with longitudinal fractures. The blue asterisks are the simulation result data points.	49
Figure 3.38	3D plot of PI as function of horizontal section length and well spacing in horizontal wells with longitudinal fractures. The blue asterisks are the simulation result data points.	51
Figure 3.39	Surface interaction of cumulative water production volume at different values of horizontal section length and well spacing and cumulative water production volume at 30 years, in horizontal wells with longitudinal fractures. The blue asterisks are the simulation result data points.	52
Figure 3.40	Change of PI at different values of well spacing at 30 years of desired flow rate production in horizontal wells with longitudinal fractures.	53
Figure 3.41	Flow vector distribution of horizontal wells with transverse fractures after one year of production. Full view on the left and zoomed in view on the right. . . .	56
Figure 3.42	3D plot of cumulative water produced volume as function of horizontal section length and well spacing in horizontal wells with transverse fractures. The blue asterisks are the simulation result data points.	56
Figure 3.43	3D plot of PI as function of horizontal section length and well spacing in horizontal wells with transverse fractures. The blue asterisks are the simulation result data points.	57
Figure 3.44	Surface interaction of cumulative water production volume at different values of horizontal section length and well spacing and cumulative water production volume at 30 years, in horizontal wells with transverse fractures. The blue asterisks are the simulation result data points.	58
Figure 3.45	Change of PI at different values of well spacing at 30 years of desired flow rate production in horizontal wells with transverse fractures.	59

LIST OF TABLES

Table 3.1	Values of variable for preliminary cases in three different permeability cases . . .	19
Table 3.2	Variables in model A (vertical well doublet system with hydraulic fractures) . . .	23
Table 3.3	Variables in model B (horizontal well doublet system with open-hole completion)	28
Table 3.4	Variables in model C (horizontal well doublet system with longitudinal fractures)	34
Table 3.5	Variables in model D (horizontal well doublet system with transverse fractures) .	40
Table 3.6	Summary of simulation cases for horizontal wells with longitudinal fractures for calculated performance measures (thermal breakthrough time, cumulative production volume, average productivity index, and average flow rate achieved in injection and production wells)	46
Table 3.7	Summary of simulation cases for horizontal wells with transverse fractures for calculated performance measures (thermal breakthrough time, cumulative production volume, average productivity index, and average flow rate achieved in injection and production wells)	54
Table A.1	Common grid system and reservoir properties of the doublet system	66
Table A.2	Common fluid properties of the doublet system	66
Table A.3	Common rock properties of the doublet system	67
Table A.4	Common well properties of the doublet system	67
Table C.1	Core measurement data for sample E053	70
Table C.2	Core measurement data for sample B526	71
Table C.3	Core measurement data for sample D485	72

NOMENCLATURE

A		affecting area, m ²
$BHP_{inj,max}$	maximum injection well bottomhole pressure, kPa	
$BHP_{prod,min}$	minimum production well bottomhole pressure, kPa	
C_{fD}	dimensionless fracture conductivity	
$C_{fD,real}$	realistic dimensionless fracture conductivity	
$C_{fD,sim}$	simulated dimensionless fracture conductivity	
C_w	water specific heat capacity, kJ/kg-°C	
C_r	rock specific heat capacity, kJ/kg-°C	
$cumV$	cumulative water production volume at breakthrough time, ×10 ⁷ m ³	
D	well spacing, m	
$D_{reservoirtop}$	depth of reservoir top, m	
h	reservoir thickness, m	
II	Injectivity Index, L/s-bar	
k	matrix permeability, mD	
k_f	fracture permeability, mD	
k_{fD}	relative fracture permeability	
$k_{f,sim}$	simulated fracture permeability, mD	
$k_{f,real}$	realistic fracture permeability, mD	
k_h	matrix horizontal permeability, mD	
k_v	matrix vertical permeability, mD	
L	length of horizontal section, m	

p_{prod}	bottomhole pressure at production well, kPa
p_{res}	average reservoir pressure, kPa
PI	Productivity Index, L/s-bar
PI_{linear}	Productivity Index from linear flow, L/s-bar
PI_{rad}	Productivity Index from radial flow, L/s-bar
Q	flow rate, m ³ /day
Δt	thermal breakthrough time, years
w	fracture width, m
w_{fD}	dimensionless fracture width
w_{sim}	simulated fracture width, m
w_{real}	realistic fracture width, m
r_{well}	wellbore radius, m
x_f	fracture half-length, m

Greek Letters

β	estimated coefficients for surface response model equation
μ	viscosity, Pa·s
ϕ	porosity
ρ_w	water density, kg/m ³
ρ_r	rock density, kg/m ³

ACKNOWLEDGMENTS

I would like to express my gratitude to my committee members: Dr. Luis E. Zerpa, Dr. Chad Augustine and Dr. Alfred W. Eustes for their professional help, advice and engagement on my research work. Furthermore I would like to thank JaeKyoung Cho for introducing me to the topic as well for the support on the way. I wish to express my sincere thanks to the support of this research work, from the U.S. Department of Energy, Office of Energy Efficiency and Renewable Energy (EERE), and Geothermal Technologies Office (GTO) under Contract No.DE-AC36-08-GO28308 with the National Renewable Energy Laboratory.

I would like to thank my friend, Xuejing Yang, for her understanding and unconditional support throughout the hard times during the process. Last but not least, I would like to say thanks to my loved husband, Hao Liu, for his support, encouragement and love for the process of the master thesis. I will be grateful forever for your love.

CHAPTER 1

INTRODUCTION

The extraction of geothermal energy in the form of hot water from sedimentary rock formations could expand the current geothermal energy resources toward new regions with the application of enhancement techniques (e.g., well hydraulic stimulation) to achieve commercial production/injection rates. Cho et al. (2015) evaluated the performance of the sedimentary geothermal reservoir using numerical reservoir modeling, which allowed studying different well configurations and productivity enhancement techniques. This thesis expanded upon this idea to develop a methodology to maximize thermal recovery from the geothermal system. A static geological model was built as the structure for reservoir simulations. The sensitivity of eight variables, which would affect the thermal evolution and hydraulic behavior of the geothermal reservoirs, were analyzed in four well configuration models. The eight variables are well type (vertical or horizontal), well spacing, length of horizontal section, hydraulic fracture direction, fracture half-length, fracture spacing, dimensionless fracture conductivity and ratio of reservoir vertical permeability to horizontal permeability. The four well configuration models, shown in Figure 3.3, are one vertical well doublet system with hydraulic fractures, and three horizontal well configurations with open-hole completion, longitudinal fractures and transverse fractures, respectively. In sensitivity analysis, the most efficient well configuration and the corresponding influential variables were selected. A response surface model (RSM) was determined by the stepwise linear regression method, then the optimal well configuration was designed by using the RSM equations.

1.1 Motivation of Study

The demand for renewable, clean and sustainable energy has become the focus of new energy research, because of the growing attention on the environmental issues and limited resources of fossil fuels. In this situation, geothermal energy becomes a potential energy resource. Geothermal energy primarily travels within the Earth by conduction and convection. This is the heat from the interior of the Earth, producing energy 24 hours a day (Blodgett and Slack 2003). The heat conductively increases the temperature of the rocks in the Earth and consequently the hot rocks

heat the surrounding aquifers. Hot water and steam formed in porous and permeable rocks may be trapped under impermeable rocks, thus forming a geothermal reservoir.

The hot water resources can be brought to the surface to generate electricity or to be used as a heating resource without combustion, thus without polluting the air. The estimated power of geothermal energy in the world is equivalent to 42 million megawatts (MW), which provides an inexhaustible supply of energy (Energy and Geosciences Institute 1997). The extraction of geothermal energy from sedimentary formations relies on heat convection carried by fluid flow through the rock matrix, where the permeability of the sedimentary rocks is a key factor to the geothermal system performance. Sedimentary formations with relatively high temperatures (~ 150 °C) can be typically found at depths ranging from 2 to 6 km. The permeability of these sedimentary formations is expected to be in the range from 1 to 100 md (Kirby 2012). Allis et al. (2011) presented a discussion on the potential of geothermal systems in stratigraphic reservoirs of the western US at depths of 3 to 5 km. They presented permeability data obtained from oil and gas activity of the Rocky Mountains and Great Basin of the US. They showed that a lower Paleozoic carbonate section has a permeability up to 70 md, while siliciclastic reservoirs have an average permeability of 30 md, both at depths of 3 to 5 km.

Cho et al. (2015) showed that sedimentary geothermal systems with vertical wells require reservoir permeabilities in the order of hundreds of millidarcies. In order to meet desired flow rates ($\sim 500 - 2000$ gpm) considering bottomhole pressure restrictions, it is required to include reservoir enhancement techniques to the geothermal system design. Reservoir enhancement techniques improve the well inflow performance required to meet desired flow rates in low permeability sedimentary rocks. Cho et al. (2015) evaluated the hydraulic and thermal performance of sedimentary geothermal systems using numerical reservoir modeling, which allowed studying different well configurations and productivity enhancement techniques. The most promising reservoir enhancement techniques obtained were horizontal wells with longitudinal hydraulic fractures or horizontal wells with multi-stage hydraulic fractures.

The lifetime of the geothermal system, when considering a well doublet, is given by the thermal breakthrough time. This is defined as the time required for the cold injected water to decrease the temperature of produced fluid below the initial reservoir temperature by one degree Celsius. An important parameter that influences the thermal breakthrough time is the well spacing, as

highlighted by Augustine (2014) using an analytic reservoir model. In the analytic model used by Augustine (2014), the thermal breakthrough time is directly proportional to the square of the well spacing, which indicates the importance of this design parameter. The thermal breakthrough time could be used as a constraint for the design of the geothermal system, by specifying a desired lifetime for the project and then determining the values of influential variables that will meet this constraint.

This research work presents a methodology to maximize thermal recovery from a sedimentary geothermal system. A commercial thermal reservoir simulator (STARS from CMG) was used to evaluate the geothermal reservoir performance using different design parameter values. The results obtained from the numerical reservoir simulations were used to build a response surface model based on the multiple linear regression method. The optimal configuration of the sedimentary geothermal systems was obtained from the analysis of the response surface model.

1.2 Objective

The research objective was to select optimal well configuration(s) in a sedimentary geothermal reservoir, which maximizes the productivity index and injectivity index by systematically changing the values of influential variables of the system, subject to a constraint of thermal breakthrough time greater than or equal to 30 years. The accomplished items are:

1. Generated a static reservoir model in the candidate formation, Lyons formation.
2. Selected the variables of interest that would affect the thermal evolution and hydraulic behavior of the geothermal reservoir.
3. Analyzed the preliminary cases in three different permeability estimations in the static geological model.
4. Modified the values of the variables for sensitivity analysis after the selection of permeability estimation.
5. Performed simulations to build the surface response models, and determined the optimal well configuration of the sedimentary geothermal system.

1.3 Methodology

To have a realistic simulation result, the geological model was developed using actual well log and core data from the candidate formation: Lyons formation in the Wattenberg field, Denver-Julesburg basin, in Colorado. The reservoir characterization involved the pre-processing and analysis of 14 well logs, obtained from the Colorado Oil and Gas Conservation Commission website, which were drilled through the Lyons formation. A geostatistical approach was used, based on the well log data, to construct a reservoir model with geologic features, such as, geometry (tops, bottom, and thickness), rock properties (i.e., porosity), and temperature. Ordinary Kriging was used in the generation of temperature distribution and surface maps of tops and bottoms. Kriging estimates an unknown property at a location of interest; the process weighs the known properties nearby for the estimation (Matheron 1963). When the mean value of all data is not known, Ordinary Kriging is used for linear data interpolation. A weighted average of the neighboring data is computed to obtain the estimate value in the new location (CMG 2011). In addition to search radius and number of nearby cells for search, Ordinary Kriging uses a variogram model from which the interpolation weights will be computed. Variogram is defined as the average of squared value of difference in data at a certain location, showing a spatial correlation of data (Cressie 1993). With an increase in the search area, more data is included for analysis.

Another geological feature, porosity, was characterized by using Sequential Gaussian Simulation (SGS). This is the method that generates N number of data in a sequential way, satisfying data covariance. Contrary to Ordinary Kriging, Sequential Gaussian Simulation estimates a mean value first, and uses it to construct the cumulative density function (cdf) for the estimation of next location and generate a new cdf. This process is repeated until the grid is full. The result model honors the available values and reproduces the corresponding histograms and correlation functions. SGS is particularly appropriate for simulating petrophysical properties such as permeability and porosity, because it captures the variability of the rock properties in a space (Verly 1993). In this model, core measurement data was used to build a correlation between porosity and permeability and to generate the permeability distribution.

With the geological model ready, eight variables of interest that would affect the hydraulic behavior (i.e., well productivity/injectivity), and thermal evolution of the reservoir (i.e., thermal

breakthrough time) are selected, as shown below:

1. well type (vertical vs. horizontal)
2. well spacing
3. length of horizontal section
4. hydraulic fracture direction
5. fracture half-length
6. fracture spacing
7. dimensionless fracture conductivity
8. ratio of reservoir vertical permeability to horizontal permeability

All simulation cases were classified into models A, B, C, and D, based on well configuration. These consist of one vertical well doublet system with hydraulic fractures and three other horizontal well configurations with open-hole completion, longitudinal fractures and transverse fractures, respectively. In each model, the simulation cases were categorized into subgroups I, II, III, etc, depending on the number of variables in that model. Under subgroups, three levels of values were assigned for each variable, so that each subgroup was broken down into three cases. Default values of the variables are mentioned in Section 3.1; and they consist of the base case in each model. In each model, each variable was modified to two other values for the sensitivity analysis to determine the most efficient well configuration(s) and the corresponding influential variables, shown in Section 3.2. Then a stepwise linear regression method was applied to determine a response surface model for the thermal evolution and hydraulic behavior of the geothermal reservoir in terms of corresponding influential variables. From there, the optimal well configuration was determined.

Simulation cases were built to run on CMG STARS to simulate geothermal production. The calculation of simulated fracture permeability, based on dimensionless fracture conductivity, is described below. Dimensionless fracture conductivity is an important design factor in the stimulation technique. It is a dimensionless factor, which is defined as the ratio of fluid transmission capacity from the fracture into the wellbore to that from the formation into the fracture (Pearson 2001).

Grids near the fractures are refined into finer resolution for a more accurate analysis. Meanwhile, the actual fracture width cannot be assigned directly because of its significantly small value in the order of nanometer. So fracture width is expressed in terms of fracture permeability according to definition of the dimensionless fracture conductivity.

Dimensionless fracture conductivity is described as the product of two dimensionless variables, dimensionless relative fracture permeability (k_{fD}) and dimensionless fracture width (w_{fD}) as shown in Equation 1.1.

$$C_{fD} = k_{fD} \times w_{fD} = \frac{k_f w}{k x_f} \quad (1.1)$$

where

$$k_{fD} = \frac{k_f}{k} \quad (1.2)$$

$$w_{fD} = \frac{w}{x_f} \quad (1.3)$$

k is the permeability of the matrix. k_f , w , x_f are the permeability, width and half-length of the fracture.

Industry expectations dictate a realistic dimensionless fracture conductivity, $C_{fD,real}$, which should equal the simulated dimensionless fracture conductivity, $C_{fD,sim}$, in Equation 1.4 and Equation 1.5.

$$C_{fD,sim} = C_{fD,real} \quad (1.4)$$

$$\frac{k_{f,sim} w_{sim}}{k x_f} = \frac{k_{f,real} w_{real}}{k x_f} \quad (1.5)$$

The realistic fracture width, w_{real} , is decided based on the field data. According to Equation 1.6, the realistic fracture permeability, $k_{f,real}$, is calculated in Equation 1.7.

$$C_{fD,real} = \frac{k_{f,real} w_{real}}{k x_f} \quad (1.6)$$

$$k_{f,real} = C_{fD,real} \frac{k x_f}{w_{real}} \quad (1.7)$$

Rearranging Equation 1.5 to Equation 1.8, $k_{f,sim}$, the simulated fracture permeability is calculated to meet $k_{f,real}$ and w_{real} , with a pre-chosen simulated fracture width, w_{sim} , as described in Appendix A.

$$k_{f,sim} = k_{f,real} \frac{w_{real}}{w_{sim}} \quad (1.8)$$

CHAPTER 2

STATIC RESERVOIR MODEL

The Lyons formation in the Wattenberg field, Denver-Julesburg Basin is chosen as the candidate geothermal reservoir. A static reservoir model is developed, with analysis of available formation data, such as well logs, bottomhole temperature, porosity and permeability from core samples. Then the “sweet spot” with high porosity and relatively high temperature is extracted out to be used as the area of research. Procedures followed during the generation of the static reservoir model are explained in this chapter.

2.1 Geothermal projects in the world

Geothermal energy has been put into production in some places. For example, in California around 3.4 percent of electric generation capacity was from geothermal resource in 2014, as shown in Figure 2.1. Other than the in-state production, California has another 700 GWh of imported geothermal power, which in total generates 6.18 percent of the state’s total system power (California Energy Commission 2015a). In California, the geothermal energy used is in two forms, dry steam and super-hot water. Geothermal projects of high heat flow are typically drilled 3 kilometers underground, which is currently economical, and they can reach a geothermal reservoir of temperature greater than or equal to 150 °C (Sass and Priest 2002).

The success of geothermal projects in California indicates the feasibility of production in geothermal reservoirs. Typically, a geothermal power plant is aimed for an economic lifetime of 30 years (Menjoz and Sauty 1982). In California, most power plants are in their early life, but they are suffering from low temperature and insufficient pressure. To transfer the hydraulic fracture techniques more efficiently to the geothermal industry, also in sedimentary geothermal reservoir, this research project focuses on the optimized design of hydraulic fracture geometry of a geothermal project in the sedimentary formation to increase the productivity and longevity of the geothermal resources.

There are three successful sedimentary geothermal power plants working in North German Basin (Schellschmidt et al. 2010). The North German Basin in the central part of the Central European Basin, is made up of sandstones, clay and carbonates, with evaporite intercalations. Three plants

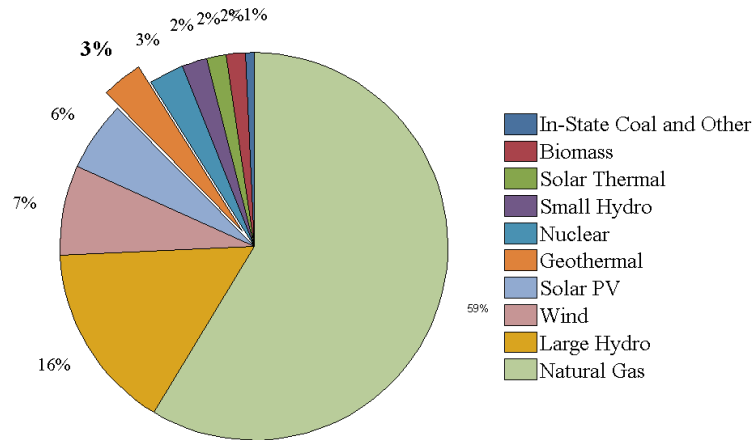


Figure 2.1: Electric Generation Capacity by Fuel Type in California, modified from California Energy Commission (2015b).

are located in the North German Basin at Neustadt-Glewe, in the Rhine Graben at Landau and in the Molasse Basin at Unterhaching. The power generation is 6.61 megawatts electrical and an additional 52.0 megawatts thermal is generated for district heating. The power production of 50,200 MWh/a ($6.61 \text{ MW} * 7600 \text{ h}$, estimated) can provide the electric consumption for about 13,200 households (with 3,800 kWh/household per year) (Schellschmidt et al. 2010).

Geothermal energy has been used in France for a variety of applications for a long time, since the 1970s, in the Paris sedimentary basin and also in Aquitaine (Sanjuan and Laplaige 2013). The Paris Basin is a large sedimentary basin which occupies a vast part of Northern France ($\sim 110,000 \text{ km}^2$) and extends northward below the English Channel, overlying deformed Carboniferous and Permian troughs in between four crystalline basement bodies. The mid-Jurassic Dogger reservoir, consisting of carbonate rocks, has been identified as the most promising geothermal development target below the urbanized Paris area (Lopez et al. 2010). France currently has two geothermal power plants: the Bouillante power plant in Guadeloupe (French West Indies) and the Enhanced Geothermal System (EGS) pilot plant in Alsace. Geothermal energy provides about 6% of Guadeloupe's electricity demand. According to the status of geothermal energy use in France, the total geothermal energy generation has increased from 56.6 GWh to 80.6 GWh from 2011 to 2013, and contributed from 0.01 % to 0.02 % to the national demand (Sanjuan and Laplaige 2013).

In southeast Hungary, geothermal wells have been used in Pannonian Basin for over 140 years. The Pannonian Basin is a large sedimentary basin in East-Central Europe. It was previously a petroleum resource system, and now can be used for geothermal production. To date, over 1,400 registered deep wells in Hungary have found thermal water, however, among them 950 are in production (Szanyi et al. 2009). The current estimated total production from thermal wells, which are mostly used about 6 months a year, is 84 million cubic meters per year (Szanyi and Kovcs 2010).

2.2 Lyons formation

The reservoir subject of this study is based on the characterization of the Lyons formation located in the Wattenberg field, Denver-Julesburg Basin, in Colorado (Figure 2.2). The Lyons formation is a Permian sandstone formation. It is composed of quartz sandstone, and has a thickness of more than 65 ft (22 m) (Hershey and Schneider 1964). The sandstone is medium grained, well sorted and of moderate rounding degree. The Wattenberg field is known to exhibit a hot-spot, with geothermal gradients up to 52 °C/km (Meyer and McGee 1985). Public data available from this field, that includes the Lyons formation, consists of some water disposal wells. The sources of information used to build the reservoir model are well logs from the Colorado Oil & Gas Conservation Commission (COGCC), core permeability data from the U.S. Geological Survey (USGS) Core Research Center, and the well bottomhole temperature from COGCC and the geothermal prospector mapping tool from the Colorado Geological Survey.

As shown in the stratigraphic column of the DJ Basin in Figure 2.3, the Lyons formation lies between the Lykins and Owl Canyon formations. The depth ranges from 2,500 to 2,800 m, with an average thickness ranging from 26 to 117 m. From outcrop observations, this formation is undisturbed by faults or fractures (Milito 2010).

2.3 Generation of static reservoir model

Data from 12 water disposal wells located in Weld County, 70 km north of Denver, was collected from well log information on the COGCC website. The depths of the top and bottom of the Lyons formation were identified from gamma ray log, and the tops and bottoms the Lyons formation were verified against well information from the Colorado Oil and Gas Information System (COGIS). With

Denver Basin

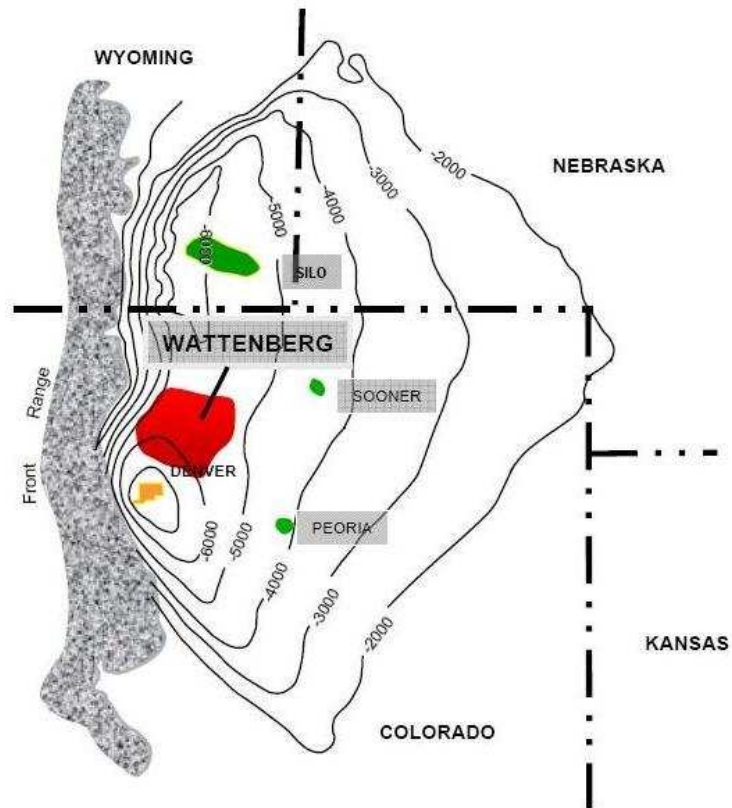


Figure 2.2: Location of Denver Basin, with Wattenberg field highlighted (Chrysoberyl 2011).

		NORTHERN FRONT RANGE, OUTCROP	ADJACENT DENVER BASIN	
QUAT.		Undifferentiated alluvial deposits	Undifferentiated alluvial deposits	
TERTIARY		Undifferentiated boulder & gravel deposits		
		Denver Formation	Castle Rock Conglomerate Dawson-Denver Formations	
UPPER CRETACEOUS		Arapahoe Formation	Arapahoe Formation	
		Laramie Formation	Laramie Formation	
		Fox Hills Sandstone	Fox Hills Sandstone	
	Pierre Shale		Richard Sandstone Mbr.	
			Terry Sandstone Mbr.	Terry "Sussex" Ss. Member
			Hygiene Sandstone Mbr.	Hygiene "Shannon" Ss. Member Sharon Springs Member
	Niobrara Formation		Smoky Hill Shale Mbr.	Smoky Hill Shale Member
			Fort Hays Limestone Mbr.	Fort Hays Limestone Member
	Niobrara Formation		Codell Sandstone Mbr.	Codell Sandstone Member
			Carlile Shale	Carlile Shale
		Greenhorn Limestone	Greenhorn Limestone	
		Graneros Shale	Graneros Shale "D" sandstone	
		Mowry Shale	Mowry Shale equivalent	
LOWER CRETACEOUS	Dakota Group	South	Muddy ("J") Sandstone	
		North		
	South Platte Fm.	Upper members, South Platte Formation	Skull Creek Shale	Skull Creek Shale
		Plainview Ss. Member	Plainview Formation	"Dakota" of drillers
		Lytle Formation	"Lakota" of drillers	
JURASSIC	Morrison Formation	Morrison Formation		
	Ralston Creek Formation	Older Jurassic rocks may be present		
	Sundance Formation			
TRI.	Jelm Formation	Jelm Formation		
PERMIAN	Lykins Formation	Lykins Formation		
	Lyons Sandstone	Lyons Sandstone		
	Owl Canyon Formation	Owl Canyon Formation		
	Ingleside Formation	Ingleside Formation		
PENNSYLVANIAN	Fountain Formation	Fountain Formation		
MISS.		Mississippian rocks		
DEV.		Devonian rocks		
SIL.		Ordovician rocks		
ORD.		Cambrian rocks		
CAM.				
PRE-CAM.		Metamorphic and intrusive rocks		

Figure 2.3: Stratigraphic Section of Rock Units in Outcrop and the Adjacent Denver Basin (Higley and Cox 2007).

the help of resistivity logs, a low permeability formation is observed below Lyons formation, which serves as an impermeable layer, and a transitional layer is observed above the Lyons formation; neither layer was part of the reservoir model. Based on the 12 well log data, surface mesh maps of the Lyons top and bottom were generated. Ordinary Kriging was used for interpolation between wells.

The temperature distribution in the Lyons formation was estimated based on information from 12 water disposal wells, using the bottomhole temperature from the well log header, and 23 production wells located in the Wattenberg field, but completed in different formations, using data from Geothermal Prospector mapping tool from National Renewable Energy Laboratory NREL (2010). The porosity distribution in the Lyons formation was calculated by using a quadratic mean of density porosity and neutron porosity values. Sequential Gaussian Simulation (SGS) was used for interpolation of porosity values between wells. Three core data sets with permeability measurements from the Lyons formation, obtained from the USGS Core Research Center, were used for the development of a porosity-permeability correlation. The permeability distribution was generated using this correlation, and the porosity distribution map from well locations. Figure 2.4 and Figure 2.5 show the temperature and porosity distribution for a selected section of the Lyons formation.

Areas A (blue) and B (red) present the highest temperature areas, with temperature of 145 °C and 137 °C, respectively. However, the porosity in area A has a maximum value of 0.07, while that of area B is 0.178. So Area B is selected due to its higher porosity (higher permeability) as the target area. At this point, the reservoir size is reduced from 28,000 km by 45,000 km to 4,500 km by 4,500 km. A static reservoir submodel is extracted out and used for later simulations. Inside the submodel, temperature varies insignificantly, so the reservoir model has a constant temperature of 137 °C in the following simulations. This submodel is called the reservoir model in this research.

CHAPTER 3

RESERVOIR SIMULATION

A commercial thermal reservoir simulator (STARS from Computer Modeling Group) was used in this work for the numerical reservoir modeling. The reservoir model was built using an orthogonal corner point grid with a resolution of $20 \times 20 \times 3.58$ meters, with ten vertical layers. The areal grid size of 20×20 meters was verified to be small enough to have an acceptable approximation to the solution of an analytic model (Cho et al. 2015). It is assumed that horizontal permeability is equal in both horizontal directions (x and y) within each grid block, while the vertical permeability is one tenth of the horizontal permeability. A single aqueous phase is considered, with density and viscosity being a function of temperature, while the thermal properties of water are constant (i.e., heat capacity, thermal conductivity). Rock properties are assumed to be constant. Details of the properties are presented in Appendix A.

The initial reservoir temperature is $137\text{ }^\circ\text{C}$ and water injection temperature is $80\text{ }^\circ\text{C}$. In some geothermal systems, with EGS technology applied, the productivity can be improved to reach flow rate of $50\text{--}70\text{ L/s}$ (Moeck 2014). The desired flow rate for injection and production are equal to 46 L/s ($4000\text{ m}^3/\text{day}$) in this research work. The desired flow rate for injection and production wells are equal to 46 L/s ($4000\text{ m}^3/\text{day}$). The maximum injection well bottomhole pressure of $35,300\text{ kPa}$ was used as a well constraint, to maintain injection pressure below the typical fracture gradient (0.60 psi/ft). The minimum production well bottomhole pressure was set to $21,300\text{ kPa}$, to prevent produced hot water from flashing into vapor. Details of the calculations of well pressure constraints are presented in Appendix B. The calculation of thermal breakthrough time is also described in Appendix B.

3.1 Preliminary cases for three permeability models

Permeability is estimated from three core-measured data of the Lyons formation, which lie outside of the area of interests considered for the reservoir model. These core data was obtained from the USGS Core Research Center. According to those measurements, the porosity-permeability correlations are developed to generate the permeability distributions in the geological reservoir

model. The general correlation equation used has the form shown in Equation 3.1.

$$k = a \times e^{b\phi} \quad (3.1)$$

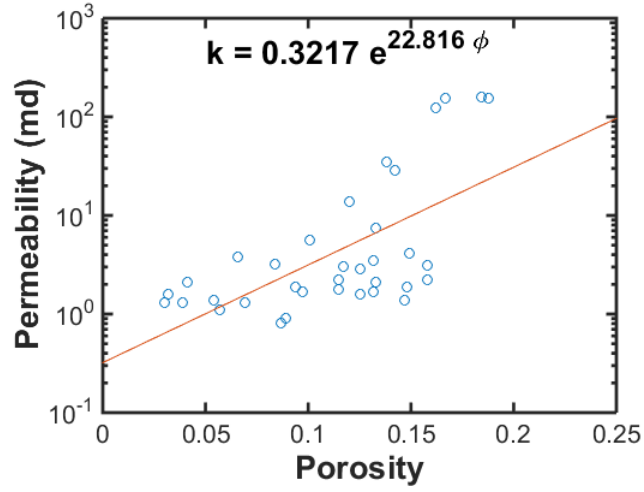
where k , ϕ are permeability and porosity, and a and b are correlation coefficients based on core sample measurements.

Based on the core samples from the USGS Core Research Center (Table C.2, Table C.1 and Table C.3 in Appendix C), there are three permeability-porosity correlations from different samples. Since permeability value is unknown in the target field, all three permeability estimates are considered independently in this research work. The permeability-porosity correlations are shown in Figure 3.1.

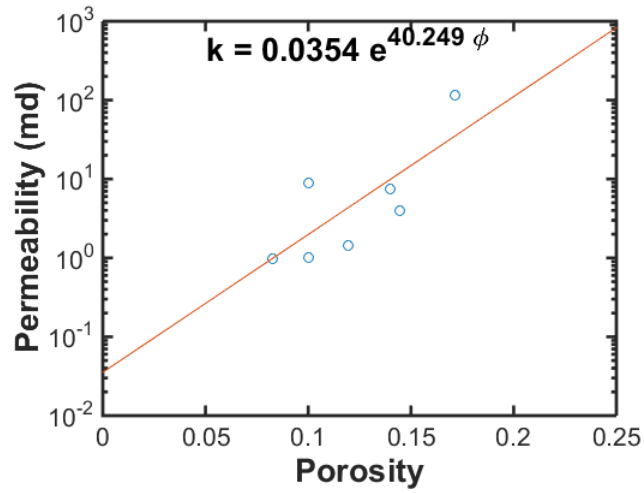
There are three static reservoir models built based on different permeability-porosity correlations from samples D485, B526 and E053. These static reservoir models have maximum values of permeability as 299md, 78md and 25.2md, respectively, so they are named high, intermediate and low permeability models. Permeability is an important factor in the production of sedimentary geothermal reservoir, so preliminary simulations are performed in each permeability reservoir model, to determine the necessity of well enhancement techniques.

According to Section 1.2, other than the base case (Figure 3.2), vertical well doublet, simulation cases are categorized into four different models. Model A is a vertical well doublet system with hydraulic fractures. Model B is a horizontal well doublet system with open-hole completion. Model C is a horizontal well doublet system with longitudinal fractures. The last one, model D is a horizontal well doublet system with multi-stage transverse fractures. One case from each model is used for the preliminary simulations for the choice of reservoir model permeability. Figure 3.3 shows the scheme of the four models.

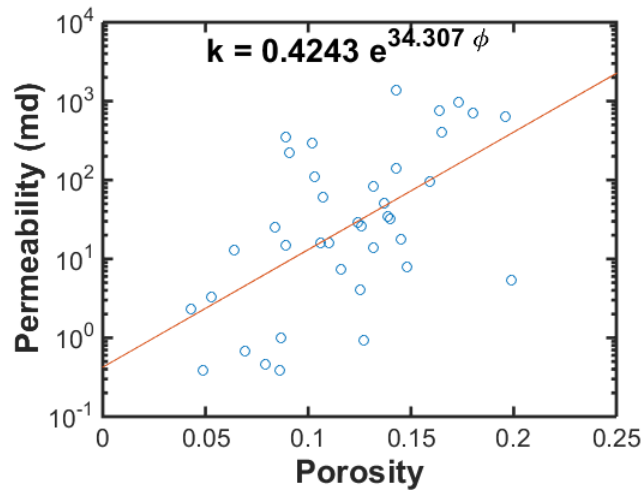
Table 3.1 shows the variable values for preliminary cases. Vertical well without fractures is the control case, as no well enhancement technique is used, named model O as the original. The following four cases are the base cases in Models A, B, C, and D. They all use the default value for each variable if applicable.



(a) Sample E053



(b) Sample B526



(c) Sample D485

Figure 3.1: Permeability-Porosity correlation for different core samples.

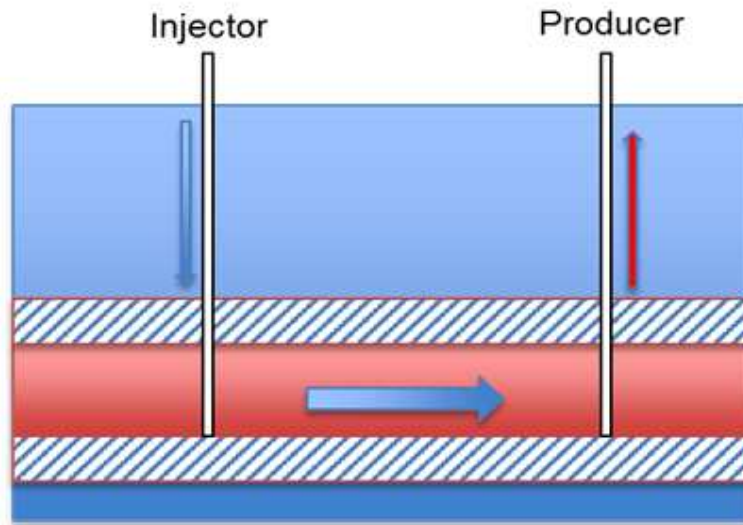
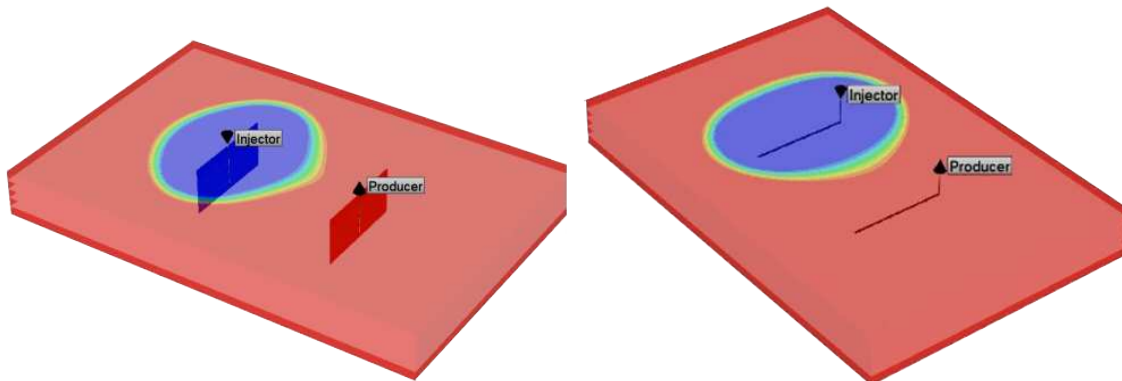
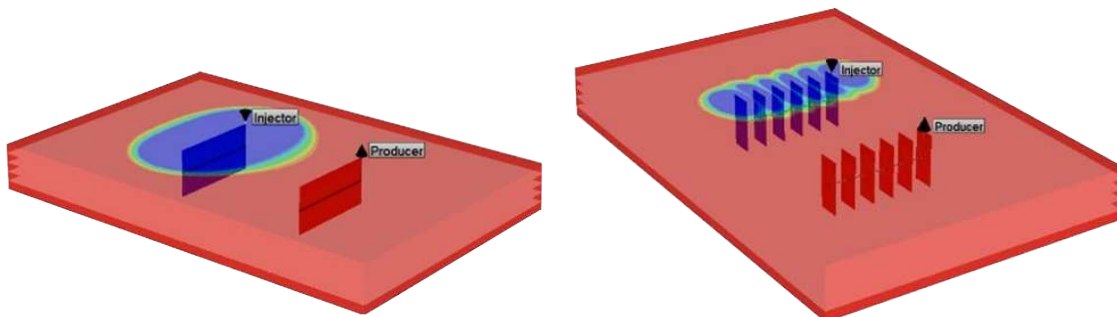


Figure 3.2: Vertical well doublet system (one injection well and one production well).



(a) Model A (vertical well doublet system with hydraulic fractures). (b) Model B (horizontal well doublet system with open-hole completion).



(c) Model C (horizontal well doublet system with longitudinal fractures). (d) Model D (horizontal well doublet system with transverse fractures).

Figure 3.3: Models A, B, C and D with different well configurations.

Table 3.1: Values of variable for preliminary cases in three different permeability cases

Model	Well configuration	Well spacing, D (m)	Length of horizontal section, L (m)	Dimensionless fracture conductivity, C_{fD}	Fracture half-length, x_f (m)	Fracture spacing, FS (m)
O	Vertical well without fractures	1500	-	-	-	-
A	Vertical well with fractures	1500	-	1.5	500	-
B	Horizontal well with open-hole completion	1500	1000	1.5	-	-
C	Horizontal well with longitudinal fractures	1500	1000	1.5	500	-
D	Horizontal well with multi-stage transverse fractures	1500	1000	1.5	500	200

3.1.1 Preliminary cases in low permeability reservoir model

Figure 3.4(a) shows the thermal breakthrough time for well doublet systems with vertical wells, vertical wells with fractures, horizontal wells with open-hole completion, horizontal wells with longitudinal fractures and horizontal wells with five transverse fractures. In low permeability reservoir model (Figure 3.4(b)), none of the preliminary cases can reach the target flow rate of 4000 m³/day. This will limit the generation of electricity from the geothermal energy production, below the desired requirement. Thermal breakthrough time is a function of the volume of reservoir affected by the flow and the rate of that flow. In this model, because of the limitation of permeability, the flow rate is limited, which limits the rate of extraction of thermal energy from the reservoir. With the restriction from well operation constraint (i.e., minimum production well bottomhole pressure), there is no good hydraulic connection between injection and production wells, so the first three cases reach thermal breakthrough after 60 years (simulations are performed to 60 years; reservoir behaviors longer than that are not observed). Based on the hydraulic behavior and thermal evolution, the application of well enhancement techniques do not improve the behavior of this low permeability reservoir model.

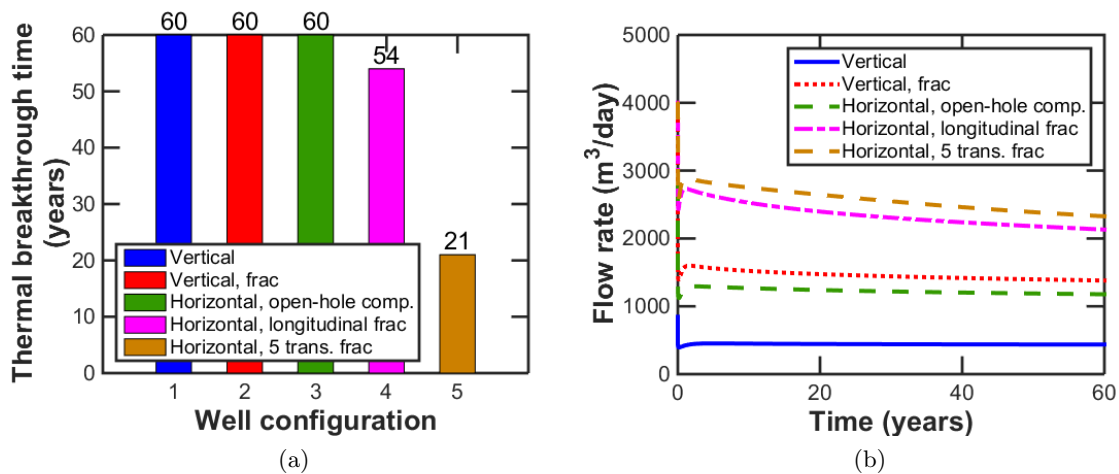


Figure 3.4: Summary of thermal breakthrough and change of production well flowrate as time changes for preliminary cases in low permeability reservoir model.

3.1.2 Preliminary cases in intermediate permeability reservoir model

Figure 3.5(a) presents the thermal breakthrough time in different cases. Vertical wells and horizontal wells without fractures reach thermal breakthrough times longer than 60 years and at 42 years, respectively, because of the poor hydraulic connection between the wells. Vertical wells with fractures, horizontal wells with longitudinal fractures, and horizontal wells with transverse fractures obtain breakthrough times of 37, 31 and 11 years, respectively. They are shorter than the values in the cases without fractures, because the existence of hydraulic fractures generates more surface area connecting the wells to the reservoir rock, which improves the system hydraulic behavior. In Figure 3.5(b), it can be seen that in vertical wells, hydraulic fracturing help to improve the production flow rate, but not meeting the desired flow rate. In horizontal wells, hydraulic fracturing increase the production flow rate almost to the desired flow rate. In vertical and horizontal wells, well enhancement techniques decrease the thermal breakthrough time, because of the improved hydraulic behavior in the reservoir. To improve hydraulic behavior and extend thermal evolution at the same time, further analysis on variables in the design of hydraulic fractures are studied in this reservoir model to determine the optimal well configuration.

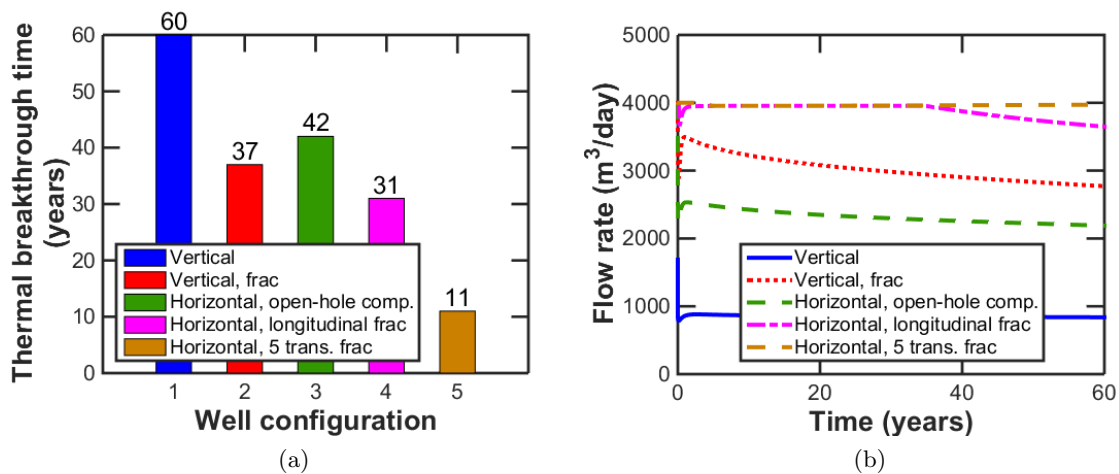


Figure 3.5: Summary of thermal breakthrough and change of production well flowrate as time changes for preliminary cases in intermediate permeability reservoir model.

3.1.3 Preliminary cases in high permeability reservoir model

For preliminary cases in high permeability reservoir model in Figure 3.6, other than vertical wells without fractures, all well configurations reach the desired flow rate throughout time and they reach thermal breakthrough at similar times. This indicates that drilling horizontal wells would provide good enough hydraulic behavior for a geothermal reservoir with a high permeability. And the application of hydraulic fracturing improves slightly on the thermal breakthrough time of the reservoir. In the high permeability static reservoir model, it is not necessary to apply well enhancement techniques, since they do not help significantly on thermal evolution or hydraulic behavior.

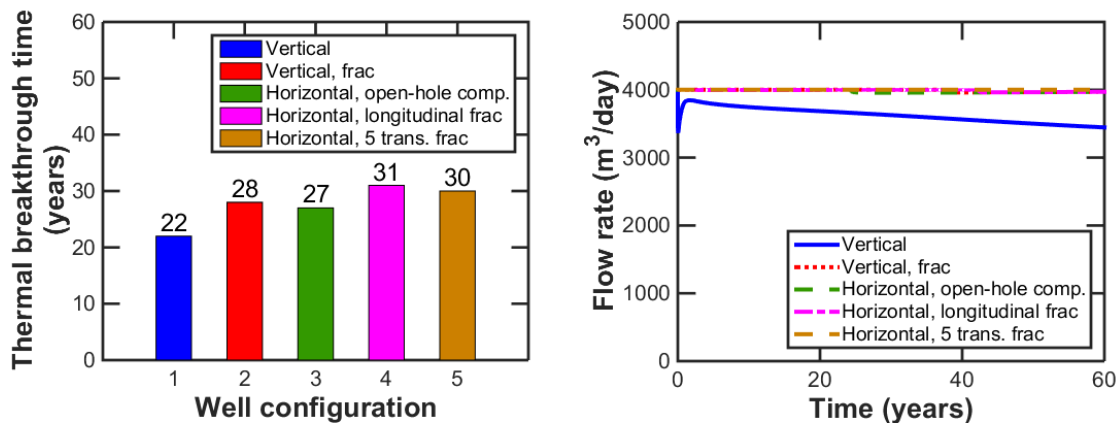


Figure 3.6: Summary of thermal breakthrough and change of production well flowrate as time changes for preliminary cases in high permeability reservoir model.

3.2 Sensitivity analysis for well configuration parameters

Based on preliminary cases in each model for the intermediate permeability reservoir model, the variable values are modified to analyze the sensitivity of each variable to the thermal evolution and hydraulic behavior of the geothermal reservoir. Variable values and corresponding results are shown in this section.

3.2.1 Model A - vertical well doublet system with hydraulic fractures

Figure 3.7 shows the well configuration and Table 3.2 shows the list of levels for all variables in model A cases.

Table 3.2: Variables in model A (vertical well doublet system with hydraulic fractures)

Model	Case #	Well spacing, D (m)	Fracture half-length, x_f (m)	Dimensionless fracture conductivity, C_{fD}	Permeability ratio, k_v/k_h
A I	1	1000	500	1.5	0.1
	2	1500			
	3	2000			
A II	4	1500	250	1.5	0.1
	5		500		
	6		750		
A III	7	1500	500	1	0.1
	8			1.5	
	9			10.0	
A IV	10	1500	500	1.5	0.01
	11				0.1
	12				1

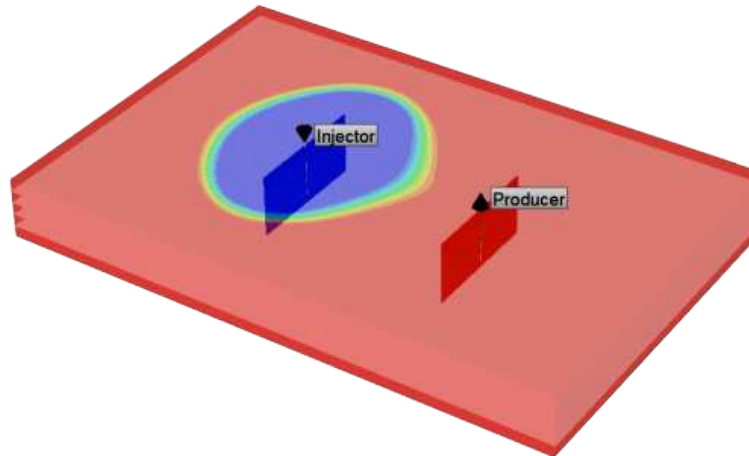


Figure 3.7: Model A (vertical well doublet system with hydraulic fractures).

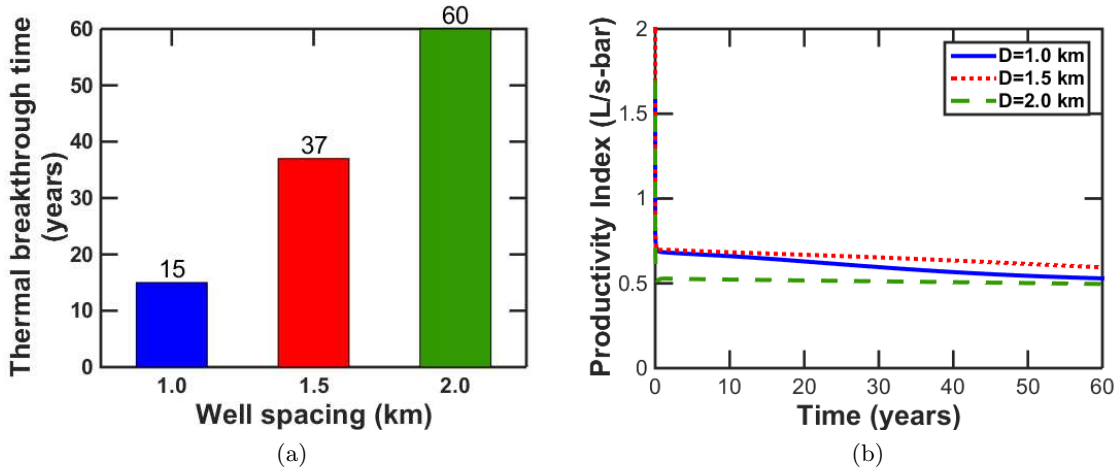


Figure 3.8: Summary of thermal breakthrough time and change of productivity index in the process of time for vertical wells with fractures cases with different well spacing values.

None of the cases in model A met the desired flow rate, which means that vertical wells with hydraulic fractures do not provide enough improvement to production. However the analysis on the variables still provided some insight that could be applied for production enhancement. Figure 3.8(a) presents that in vertical wells with hydraulic fractures, the farther the two wells are, the longer the thermal breakthrough time is. Because it increases the volume of reservoir that the fluid flows through. This increases the amount of thermal energy recovered. However, Figure 3.8(b) displays that as well spacing increases, productivity index decreases. This is because a farther well spacing leads to more resistance from the reservoir matrix to the flow.

Figure 3.9(b) shows that productivity index does not improve any more as fracture half-length reaches 500 m. As shown in Figure 3.10, the fluid forms a radial flow around the vertical wellbore, so over certain value, the increase in fracture half-length no longer helps to improve the production. Because the matrix permeability at the fracture tip is lower (Figure 3.10(d)) and the fluid tends to flow toward the production well instead of along the fracture. However, some flow is deviated along the fracture direction, so case 3 has a longer thermal breakthrough time compared to case 2, as shown in Figure 3.9(a).

Figure 3.11 shows the effect of dimensionless fracture conductivity. Higher dimensionless fracture conductivity, meaning the fracture to be more conductive, decreases the thermal breakthrough time (Figure 3.11(a)) and improves the hydraulic behavior (Figure 3.11(b)). As can be seen in Fig-

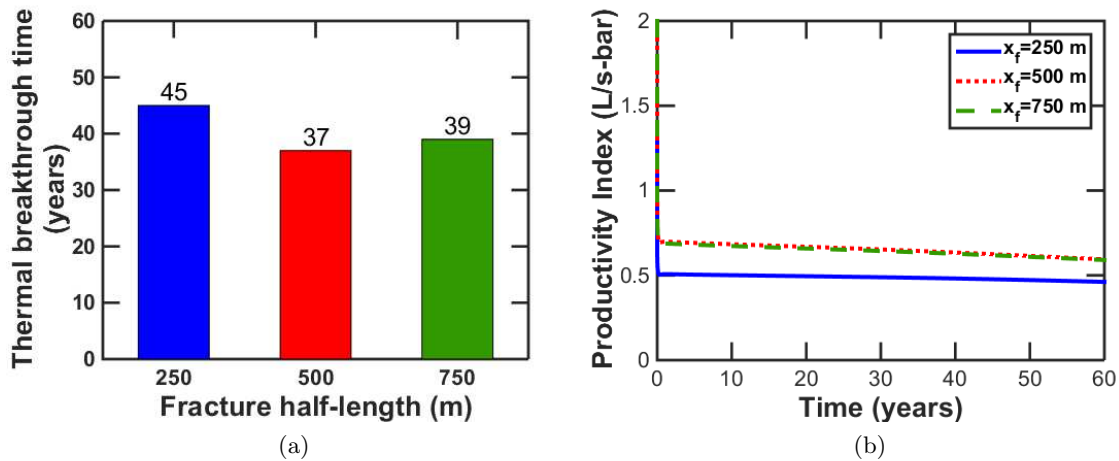


Figure 3.9: Summary of thermal breakthrough time and change of productivity index in the process of time for vertical well with fractures cases with different fracture half-length values.

ure 3.12, as the value of dimensionless fracture conductivity increases, the flow rate is higher, so thermal breakthrough arrives earlier.

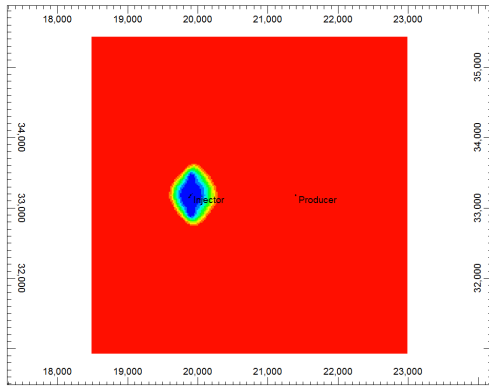
Figure 3.13 shows that the ratio of reservoir vertical permeability to horizontal permeability in the reservoir does not effect the thermal evolution or the hydraulic behavior, since the flow is mainly horizontal.

3.2.2 Model B - horizontal well doublet system with open-hole completion

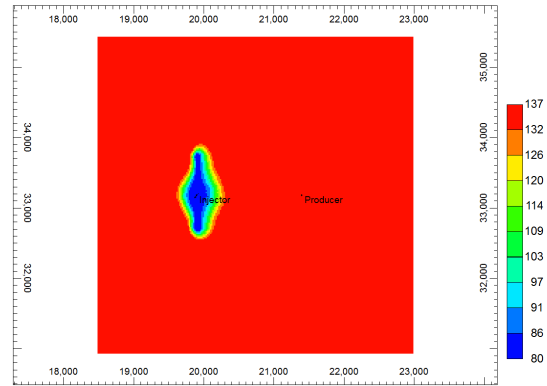
Figure 3.14 shows the well configuration and Table 3.3 shows the list of levels for all variables in model A cases. None of the cases met the desired flow rate of 4000 m³/day, indicating that horizontal wells with open-hole completion could not provide enough improvement in this geothermal reservoir. However, the sensitivity of well spacing and horizontal section length can provide the importance of well configuration for producing in horizontal wells with fractures. And the analysis of permeability ratio emphasizes the importance of reservoir heterogeneity in horizontal wells with open-hole completion.

Horizontal wells without hydraulic fractures have longer thermal breakthrough time and lower productivity index values, as the well spacing increases (Figure 3.15).

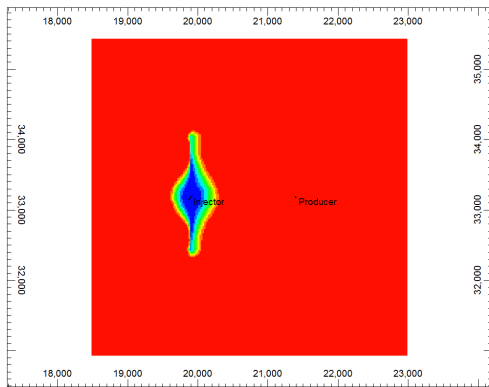
Figure 3.16 shows that longer horizontal section length is more favorable for productivity, but has insignificant effect on the thermal breakthrough time result. In horizontal wells with open-hole



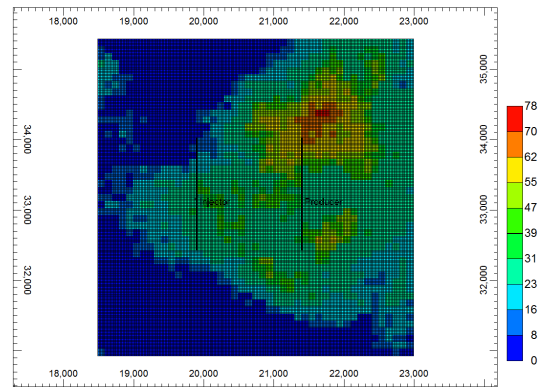
(a) $x_f = 250$ m



(b) $x_f = 500$ m



(c) $x_f = 750$ m



(d) $x_f = 750$ m

Figure 3.10: Aerial view temperature distribution after 5 years of production for vertical wells with fractures, with fracture half-lengths of 250 m (a), 500 m (b) and 750 m (c), and aerial view permeability distribution for vertical wells with fractures, with fracture half-length of 750 m (d).

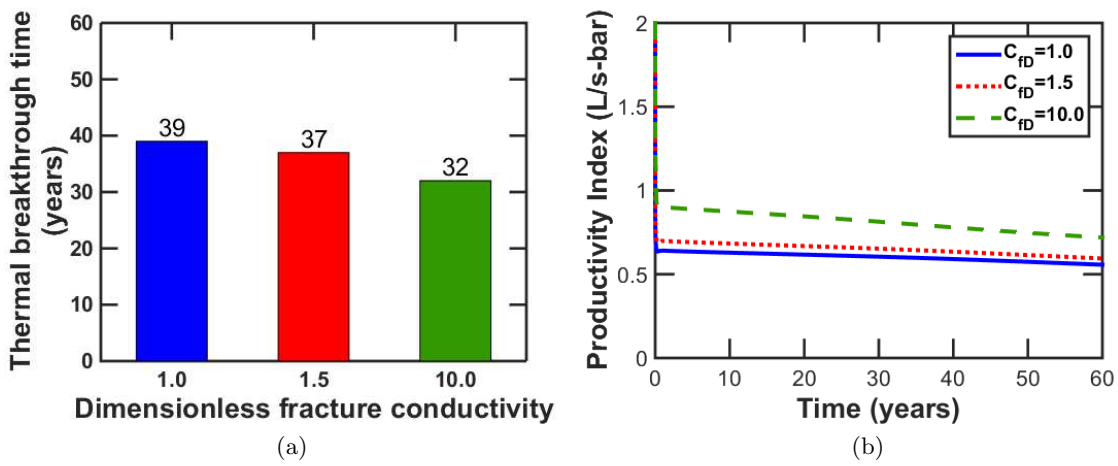


Figure 3.11: Summary of thermal breakthrough time and change of productivity index in the process of time for vertical well with fractures cases with different dimensionless fracture conductivity values.

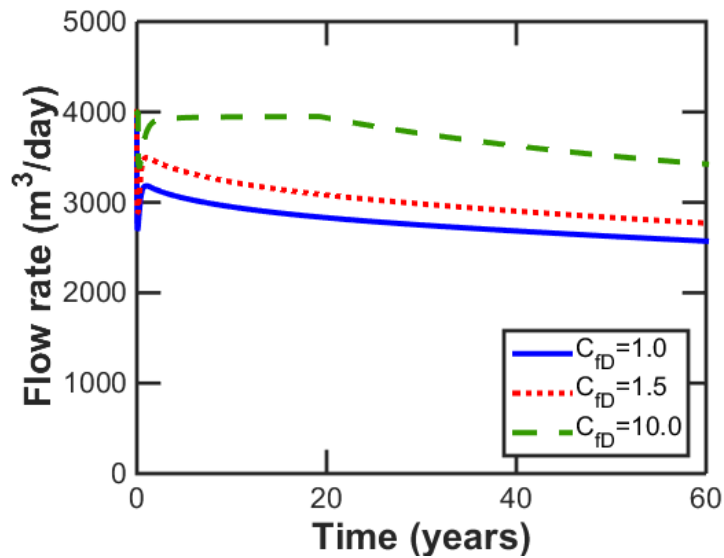


Figure 3.12: Production flow rate as function of time for vertical well with fractures cases with different dimensionless fracture conductivity values.

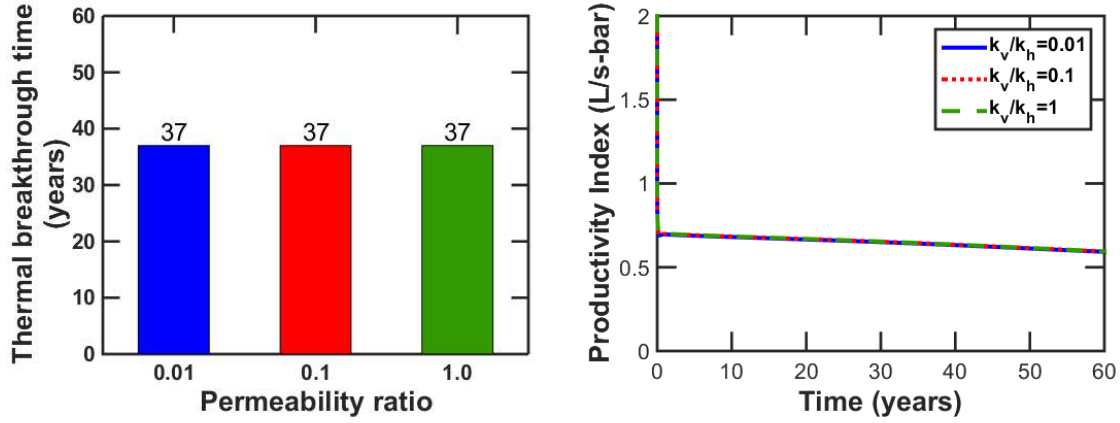


Figure 3.13: Summary of thermal breakthrough time and change of productivity index in the process of time for vertical well with fractures cases with different ratio of reservoir vertical permeability to horizontal permeability values.

Table 3.3: Variables in model B (horizontal well doublet system with open-hole completion)

Model	Case #	Well spacing, D (m)	Length of horizontal section, L (m)	Permeability ratio, k_v/k_h
B I	1	1000	1000	0.1
	2	1500		
	3	2000		
B II	4	1500	1500	0.1
	5		1000	
	6		2000	
B III	7	1500	1000	0.01
	8			0.1
	9			1

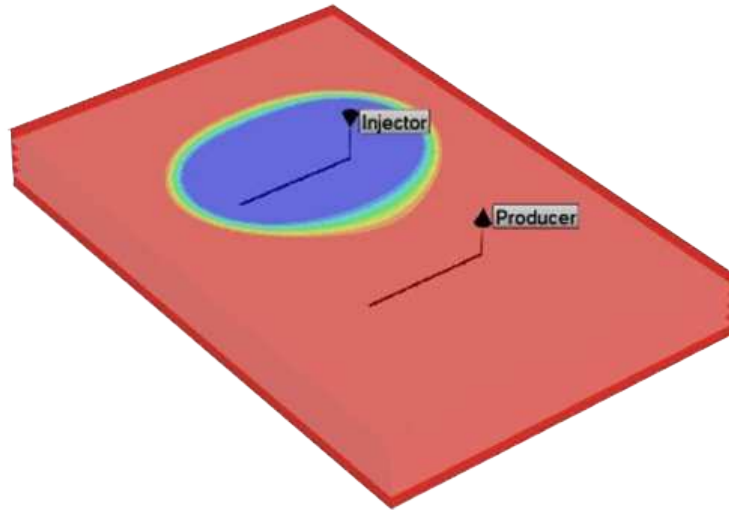


Figure 3.14: Model B (horizontal well doublet system with open-hole completion).

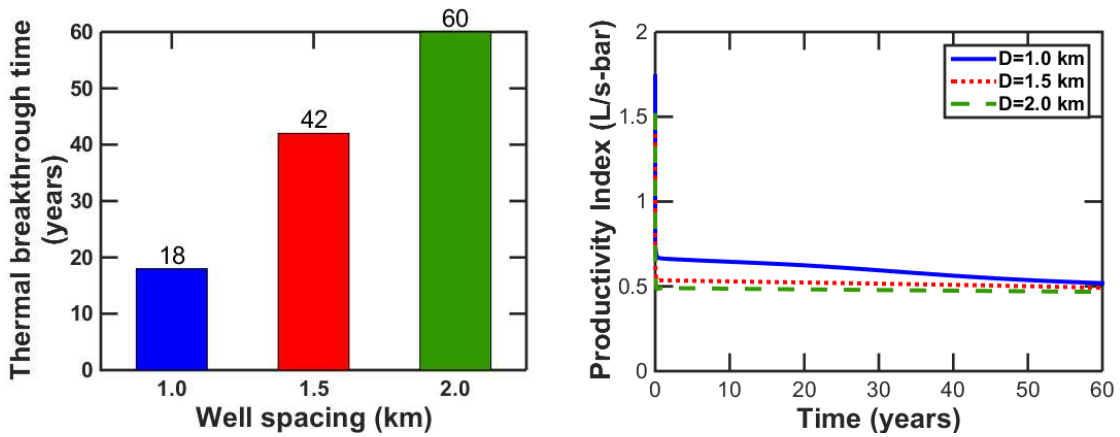


Figure 3.15: Summary of thermal breakthrough time and change of productivity index in the process of time for horizontal wells with open-hole completion cases with different well spacing values.

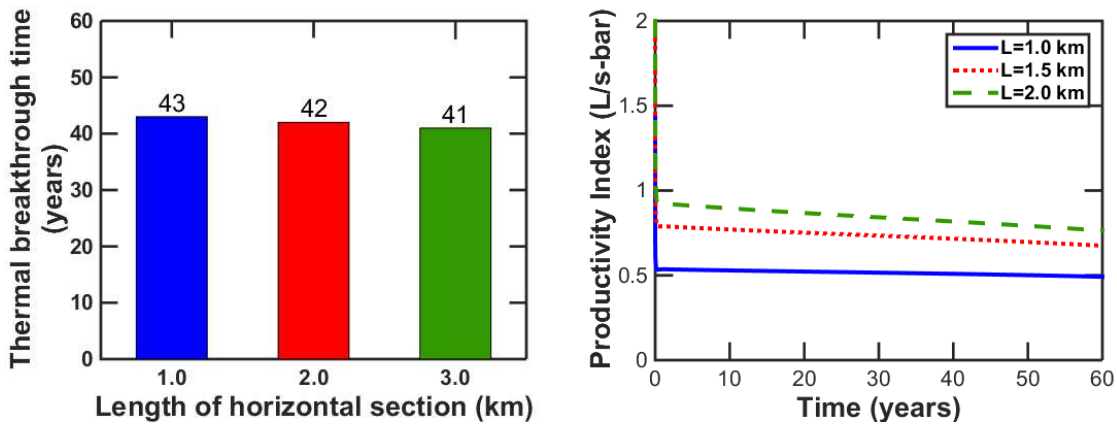
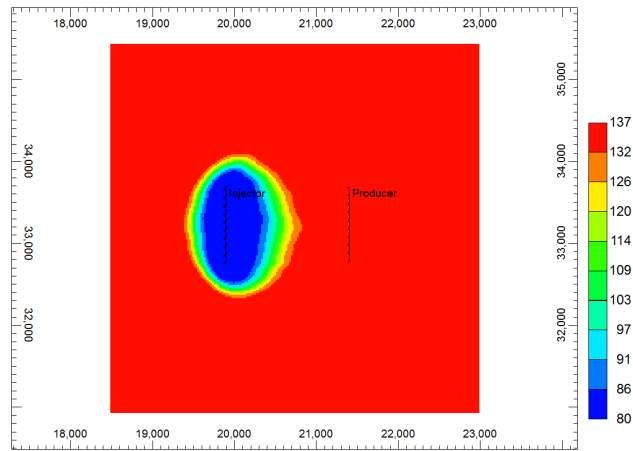


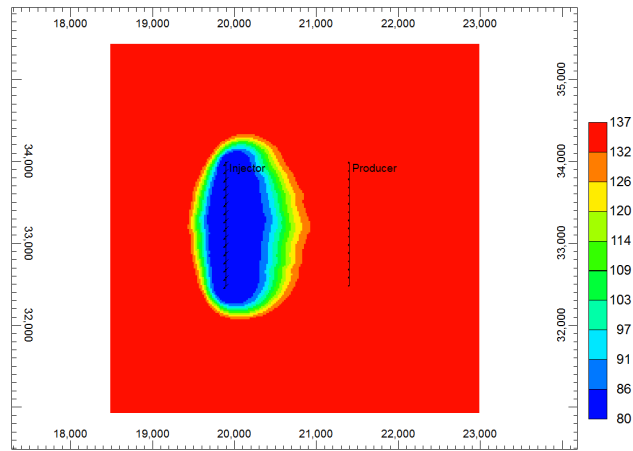
Figure 3.16: Summary of thermal breakthrough time and change of productivity index in the process of time for horizontal wells with open-hole completion cases with different horizontal section length values.

completion, with the same well spacing, a longer horizontal section length creates a larger sweeping area for the flow, thus enhancing the flow rate and sequentially productivity index, as shown in Figure 3.17. Thermal breakthrough time is a combined result from of flow rate, sweeping volume and reservoir porosity. Cases 4, 5, and 6 have different flow rates, sweeping areas, and porosity distribution of its sweeping volume, so the result of thermal breakthrough time differences cannot be explained solely by the different values of length of horizontal section. However, it indicates that the length of horizontal section would affect the thermal evolution in a reservoir system with horizontal wells, which would be invested further in models C and D in the following sections.

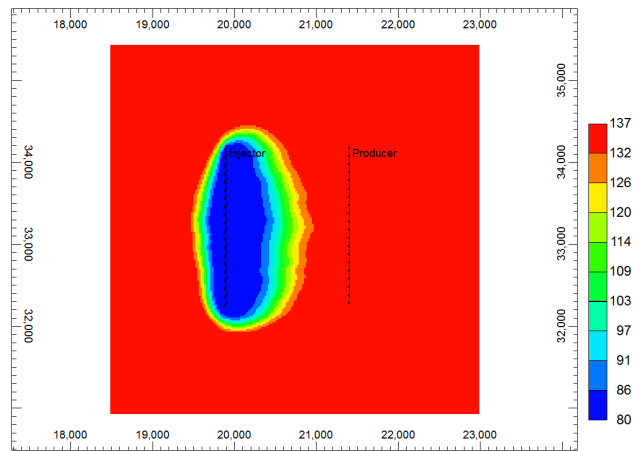
In wells without hydraulic fracturing, ratio of reservoir vertical permeability to horizontal permeability is extremely important, by shortening thermal breakthrough and increasing productivity index (Figure 3.18). With same horizontal permeability distribution, a higher ratio value provides more vertical flow in the reservoir, as shown in Figure 3.19. Or said another way, a lower ratio confines flow to the layers around the horizontal well, meaning less volume is accessed and the flow short circuits and accesses a smaller portion of the reservoir. If flow rate were held constant for all the cases (rather than being determined by the pressure restrictions) a lower ratio would give a shorter thermal breakthrough time.



(a) $L = 1.0$ km



(b) $L = 1.5$ km



(c) $L = 2.0$ km

Figure 3.17: Aerial view temperature distribution after 30 years of production for horizontal wells with open-hole completion, with horizontal section lengths 1.0 km (a), 1.5 km (b), and 2.0 km (c).

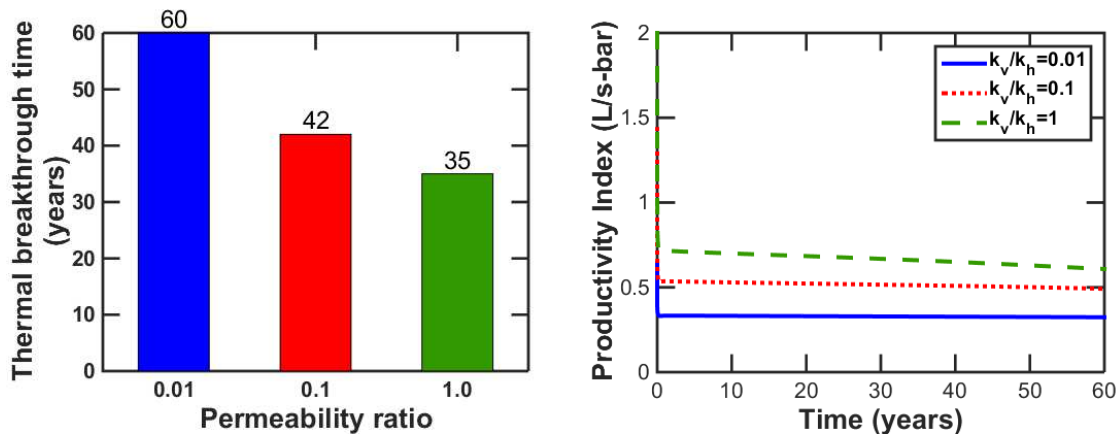


Figure 3.18: Summary of thermal breakthrough time and change of productivity index in the process of time for horizontal well with open-hole completion cases with different ratio of reservoir vertical permeability to horizontal permeability values.

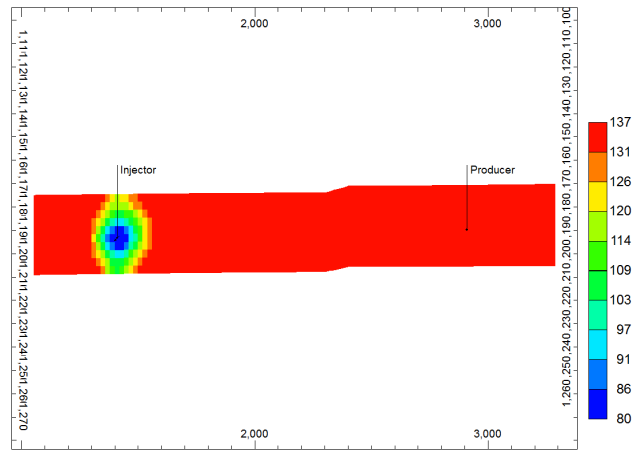
3.2.3 Model C - horizontal well doublet system with longitudinal fractures

Model C (Table 3.4 and Figure 3.20) is a horizontal well with longitudinal fractures. Here, well spacing, length of horizontal section, dimensionless fracture conductivity and ratio of reservoir vertical permeability to horizontal permeability are the studied variables. Besides case 3, all cases met desired flow rate. Based on sensitivity analysis, well spacing and horizontal section length are the influential variables, and they will be investigated into further optimization analysis.

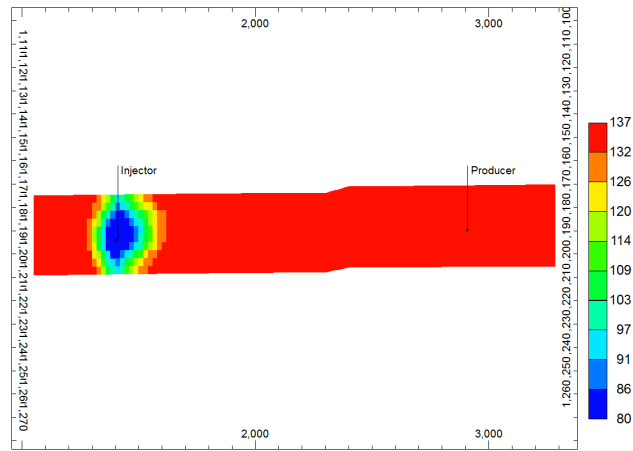
Figure 3.21 demonstrates results of cases 1, 2 and 3 in model C. It is clear that a farther well spacing increases the thermal breakthrough, but could lead to a lower flow rate and hurt the productivity index. Also, cases 1 and 2 meet the desired flow rate, while case 3 not because the wells are too far away from each other. So well spacing is an influential variable in model C and will be investigated into further analysis.

Figure 3.22 proves that a longer horizontal section length provides a longer thermal breakthrough, and increase the productivity index. The change of horizontal section length affects the flow rate and pressure drop distribution in the reservoir in a complex manner. So horizontal section length is an influential variable in model C and will be investigated into further analysis.

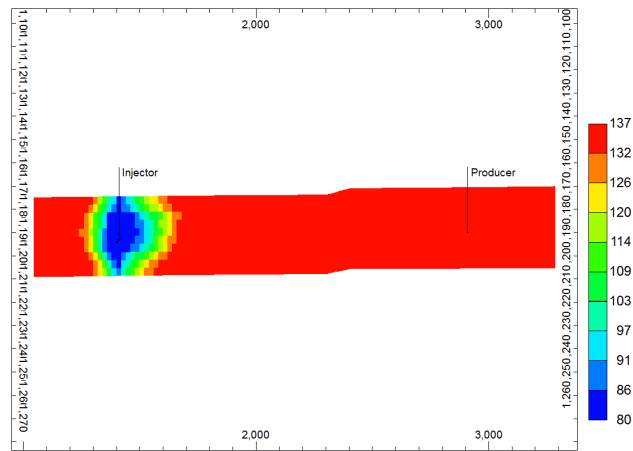
Figure 3.23 specifies the effect of dimensionless fracture conductivity on horizontal wells with longitudinal fractures. Since the fracture is longitudinal to the well horizontal section, the fluid is distributed through the fracture with help of the well horizontal section (Figure 3.24), and the



(a) $k_v/k_h=0.01$



(b) $k_v/k_h=0.1$



(c) $k_v/k_h=1$

Figure 3.19: Zoomed lateral view temperature distribution after 3 years of production for horizontal wells with open-hole completion, with ratio of reservoir vertical permeability to horizontal permeability values of 0.01 (a), 0.1 (b), and 1 (c).

Table 3.4: Variables in model C (horizontal well doublet system with longitudinal fractures)

Model	Case #	Well spacing, D (m)	Length of horizontal section, L (m)	Dimensionless fracture conductivity, C_{fD}	Permeability ratio, k_v/k_h
C I	1	1000	1000	1.5	0.1
	2	1500			
	3	2000			
C II	4	1500	2000	1.5	0.1
	5		1000		
	6		3000		
C III	7	1500	1000	1	0.1
	8			1.5	
	9			10.0	
C IV	10	1500	1000	1.5	0.01
	11				0.1
	12				1

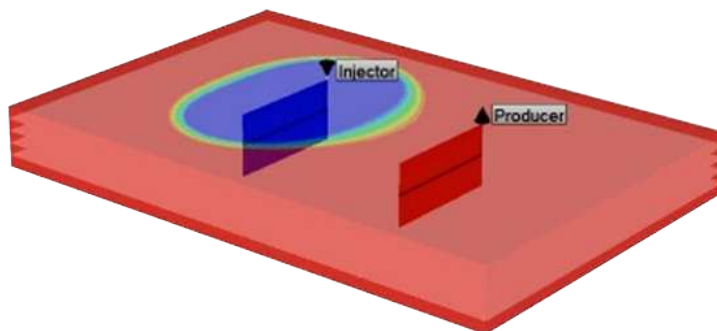


Figure 3.20: Model C (horizontal well doublet system with longitudinal fractures).

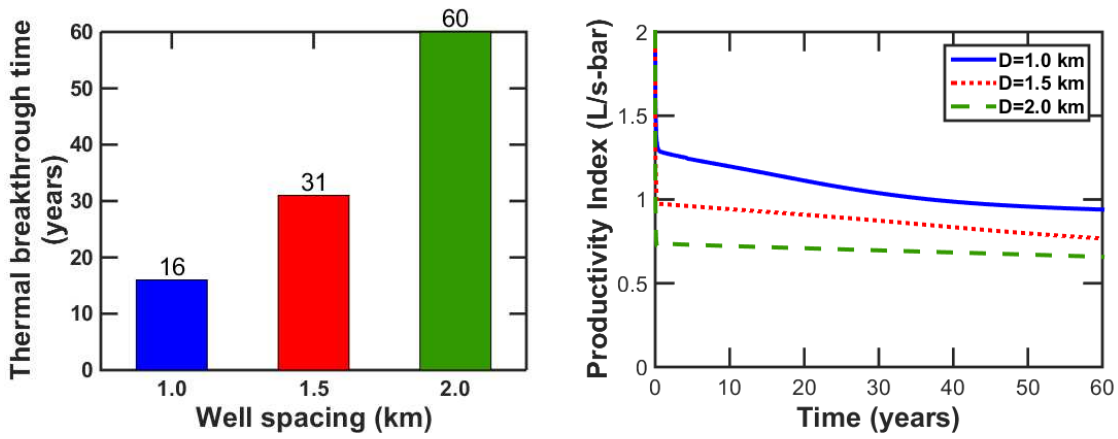


Figure 3.21: Summary of thermal breakthrough time and change of productivity index in the process of time for horizontal well with longitudinal fractures cases with different well spacing values.

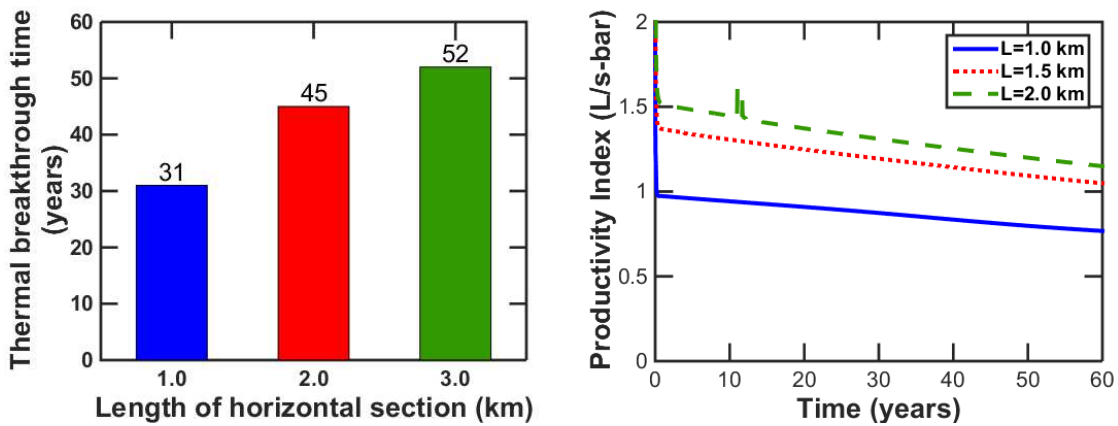


Figure 3.22: Summary of thermal breakthrough time and change of productivity index in the process of time for horizontal well with longitudinal fractures cases with different horizontal section length values.

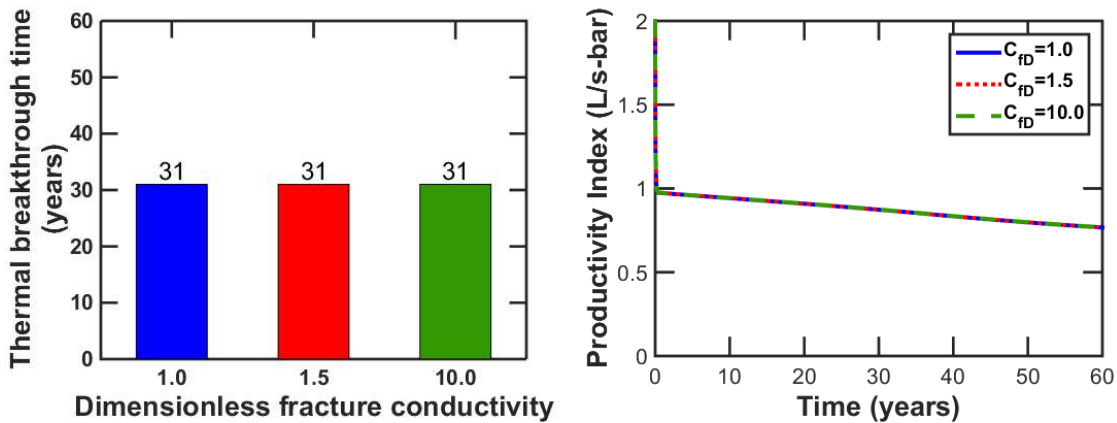


Figure 3.23: Summary of thermal breakthrough time and change of productivity index in the process of time for horizontal well with longitudinal fractures cases with different dimensionless fracture conductivity values.

value of the dimensionless fracture conductivity is not influential.

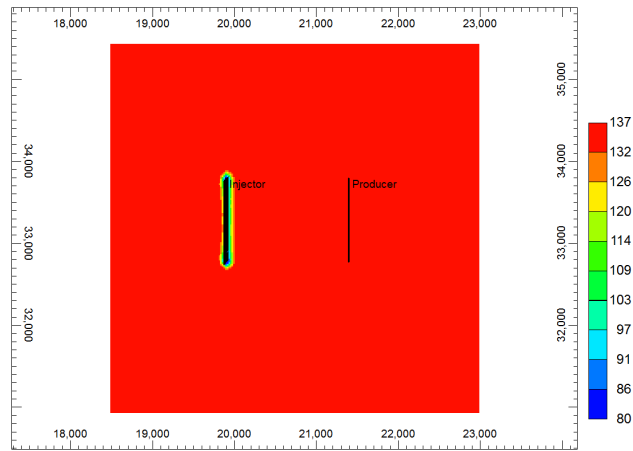
Similar to cases in model A, Figure 3.25 proves that reservoir permeability ratio brings no effect to well configurations with hydraulic fractures, because the flow is horizontal.

3.2.4 Model D - horizontal well doublet system with transverse fractures

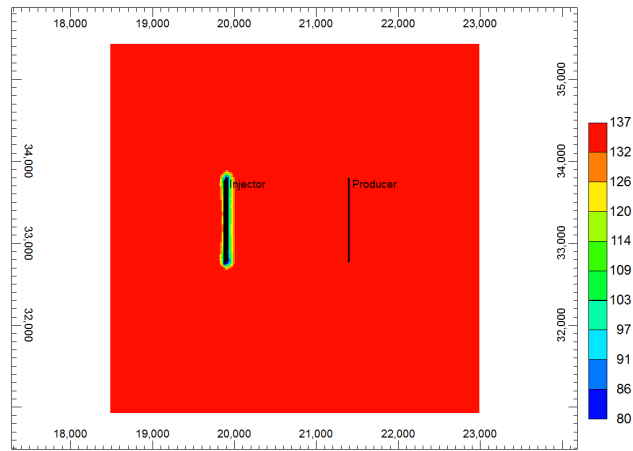
In model D, besides case 10, all cases met desired flow rate, thanks to the application of hydraulic fractures. Well spacing, fracture half-length, horizontal section length, fracture spacing and dimensionless fracture conductivity have either significant or minor effect on the reservoir. But the reservoir permeability ratio has no impact for horizontal wells with multi-stage transverse fractures. The simulation cases are shown in Table 3.5 and the well configuration are displayed in Figure 3.26.

As the distance between the wells gets widened, thermal breakthrough time increases and productivity index decreases (Figure 3.27). This is the same trend in all four models.

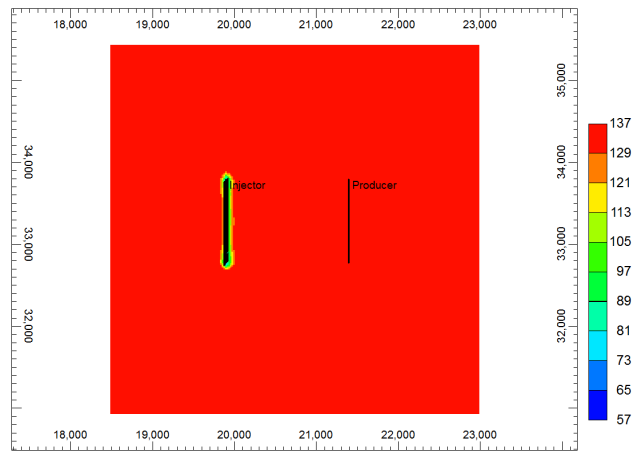
In horizontal wells with transverse fractures, the tips of the fractures shorten the effective well spacing (Figure 3.26) and cuts down the thermal breakthrough time. However, with a longer fracture half-length, more fluid flows via the fractures and raises the productivity of the well (Figure 3.28).



(a) $C_{fD} = 1.0$



(b) $C_{fD} = 1.5$



(c) $C_{fD} = 10.0$

Figure 3.24: Aerial view temperature distribution after 1 year of production for horizontal well with longitudinal fractures cases with dimensionless fracture conductivity values of 0.01 (a), 0.1 (b) and 1 (c).

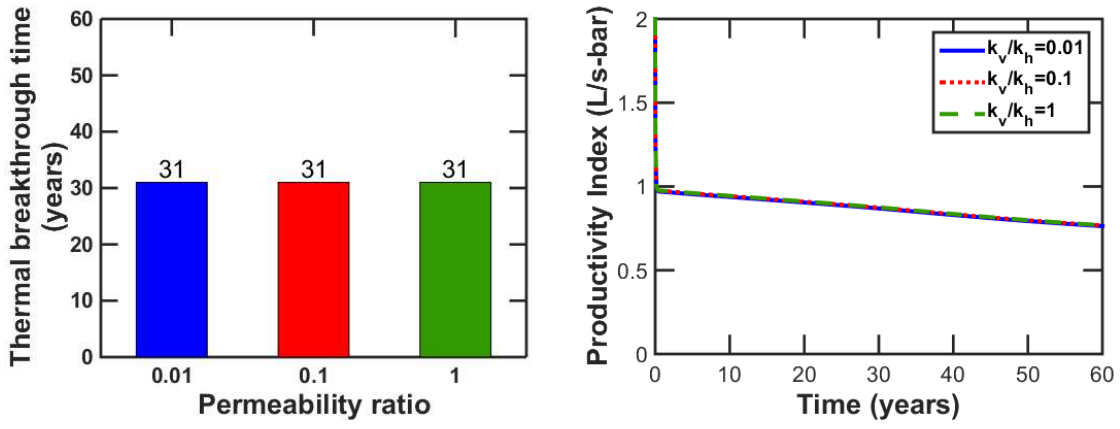


Figure 3.25: Summary of thermal breakthrough time and change of productivity index in the process of time for horizontal well with longitudinal fractures cases with different ratio of reservoir vertical permeability to horizontal permeability values.

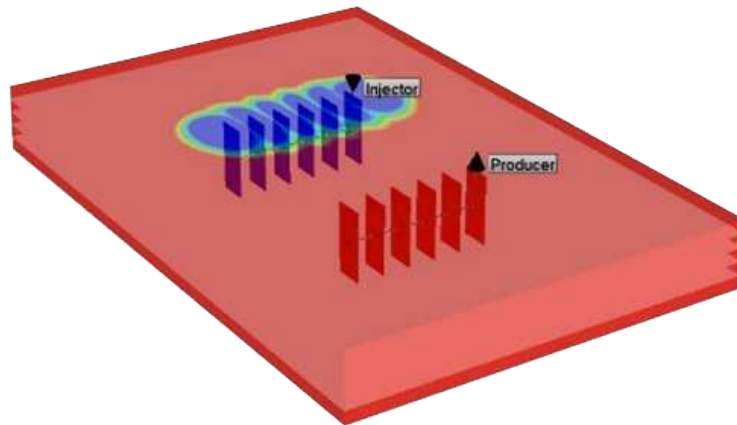


Figure 3.26: Model D (horizontal well doublet system with transverse fractures).

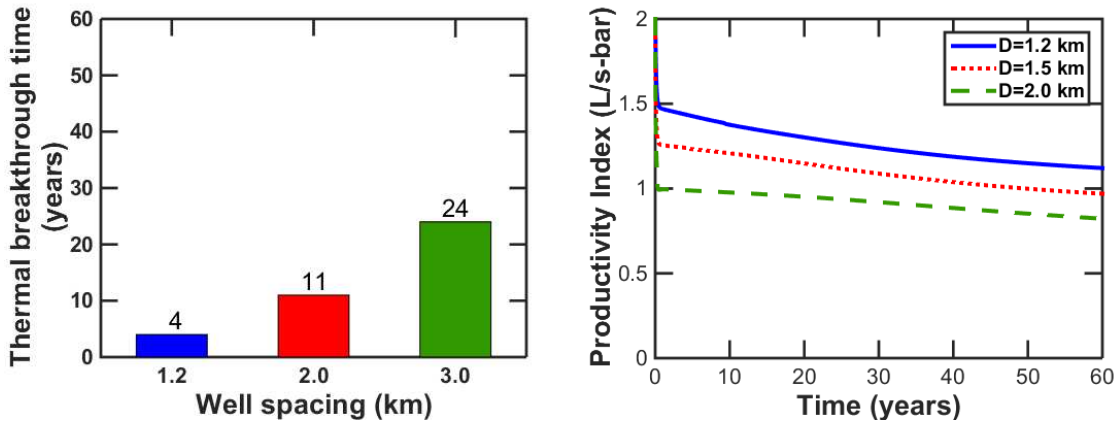


Figure 3.27: Summary of thermal breakthrough time and change of productivity index in the process of time for horizontal well with transverse fracture cases with different well spacing values.

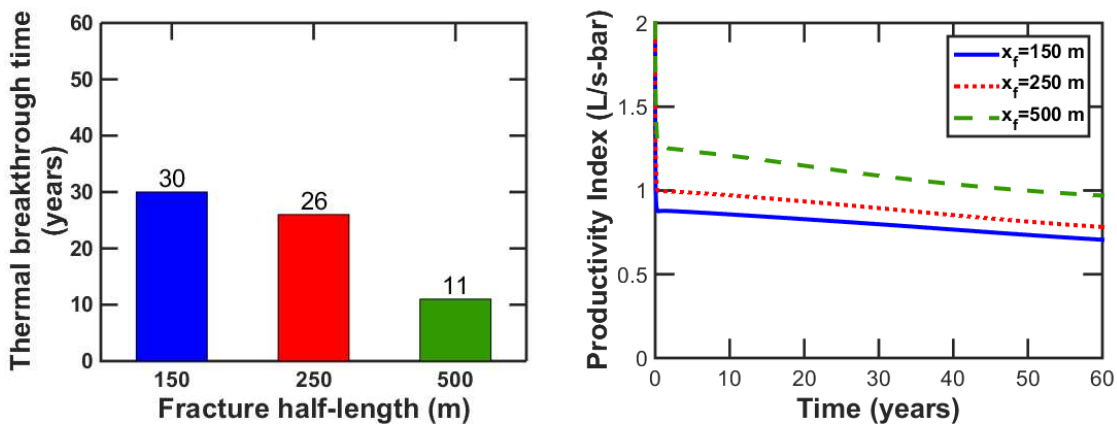


Figure 3.28: Summary of thermal breakthrough time and change of productivity index in the process of time for horizontal well with transverse fracture cases with different fracture half-length values.

Table 3.5: Variables in model D (horizontal well doublet system with transverse fractures)

Model	Case #	Well spacing, D (m)	Fracture half-length, x_f (m)	Length of horizontal section, L (m)	Fracture spacing, FS (m)	Dimensionless fracture conductivity, C_{fD}	Permeability ratio, k_v/k_h
D I	1	1200	500	1000	200	1.5	0.1
	2	1500					
	3	2000					
D II	4	1500	125	1000	200	1.5	0.1
	5		500				
	6		250				
D III	7	1500	500	2000	200	1.5	0.1
	8			1000			
	9			3000			
D IV	10	1500	500	1000	0	1.5	0.1
	11				200		
	12				100		
D V	13	1500	500	1000	200	1	0.1
	14					1.5	
	15					10.0	
D VI	16	1500	500	1000	200	1.5	0.01
	17						0.1
	18						1

Figure 3.29 points out the importance of horizontal section length in model D. With same fracture spacing, a longer horizontal section length produces more fractures along the well and opens more channels for the fluid, thus increasing productivity index. Also, a longer horizontal section enlarges the sweeping area for the flow and delays thermal breakthrough.

Case 10 (fracture spacing of zero) is the case with only one transverse fracture, since there is no other fractures to calculate the fracture spacing. As can be seen in Figure 3.31, single transverse fracture case did not meet the target flow rate, leading to a low productivity index. Fracture spacing of case 12 is half of that in case 11, meaning the number of fractures are doubled. This offers a more productive well, while not shortening the thermal breakthrough time significantly, shown in Figure 3.30.

Figure 3.32 displays the effect of dimensionless fracture conductivity. Similar to cases in model A, higher dimensionless fracture conductivity value induces fractures that are more conductive

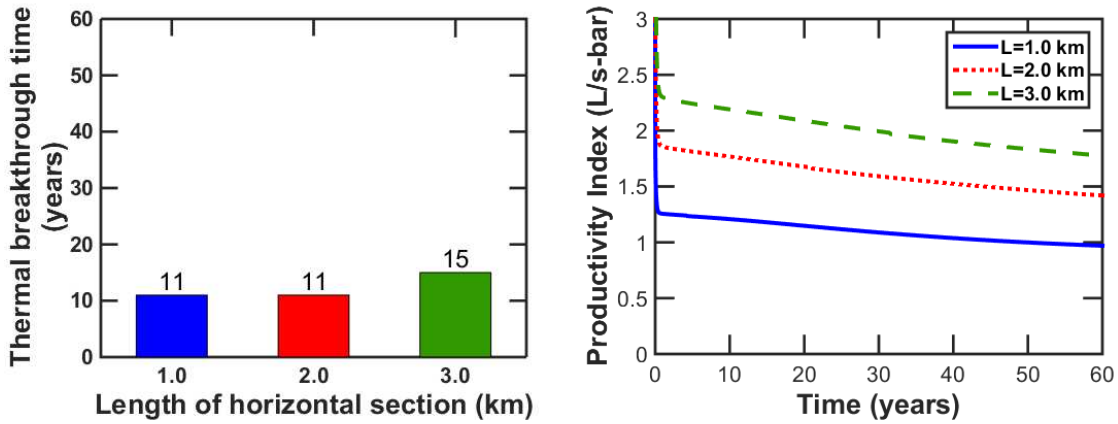


Figure 3.29: Summary of thermal breakthrough time and change of productivity index in the process of time for horizontal well with transverse fracture cases with different horizontal section length values.

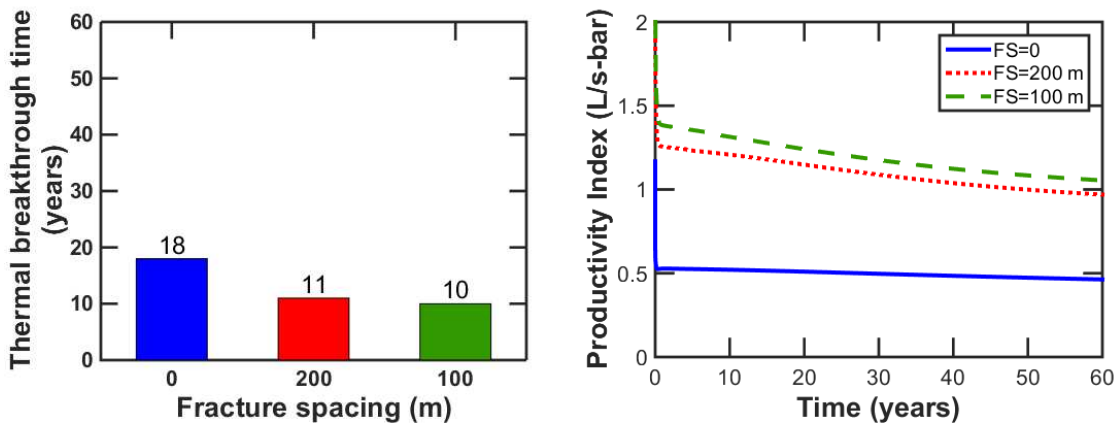


Figure 3.30: Summary of thermal breakthrough time and change of productivity index in the process of time for horizontal well with transverse fracture cases with different fracture spacing values.

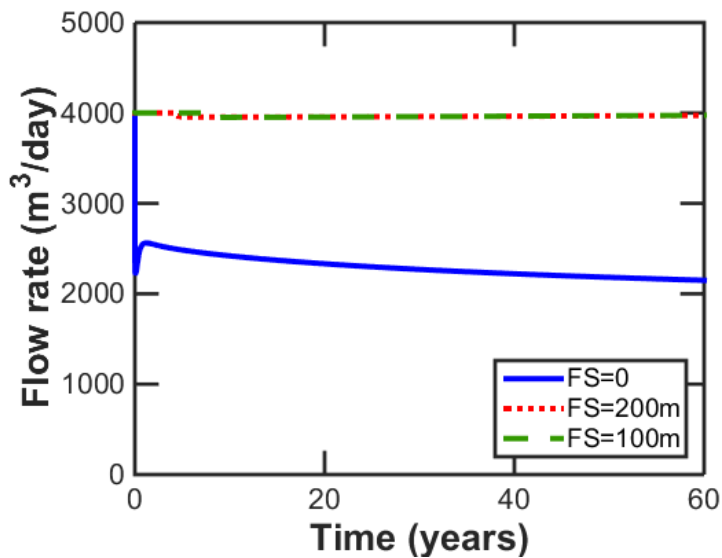


Figure 3.31: Change of production well flow rate as time changes for horizontal well with transverse fracture cases with different fracture spacing values.

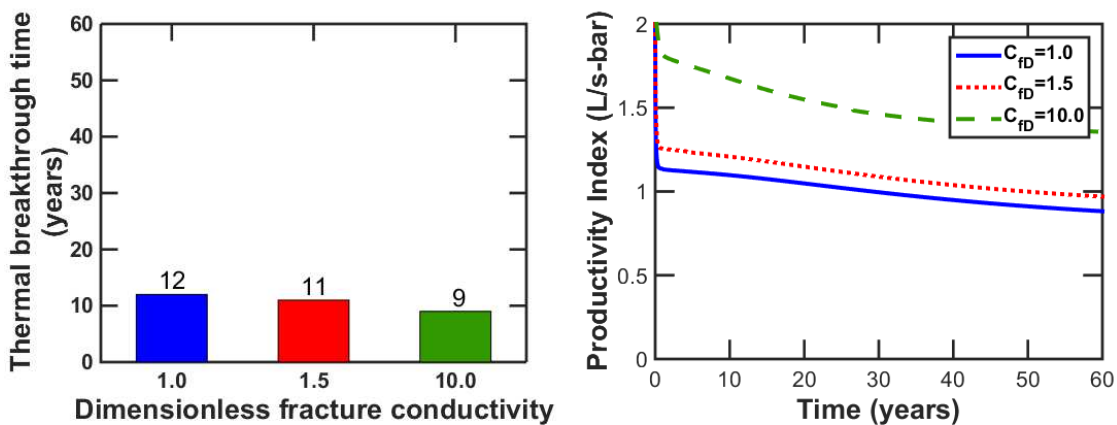
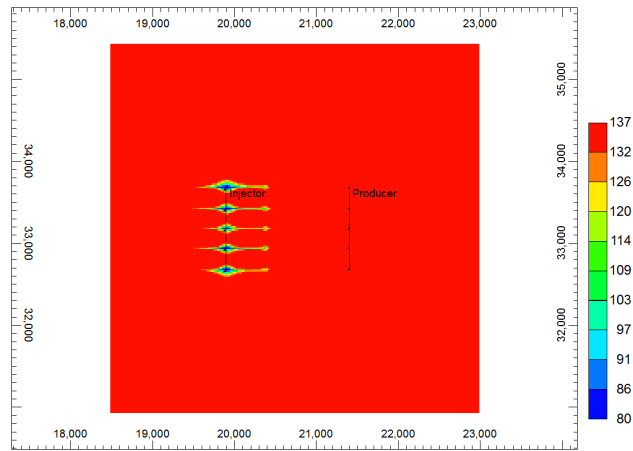
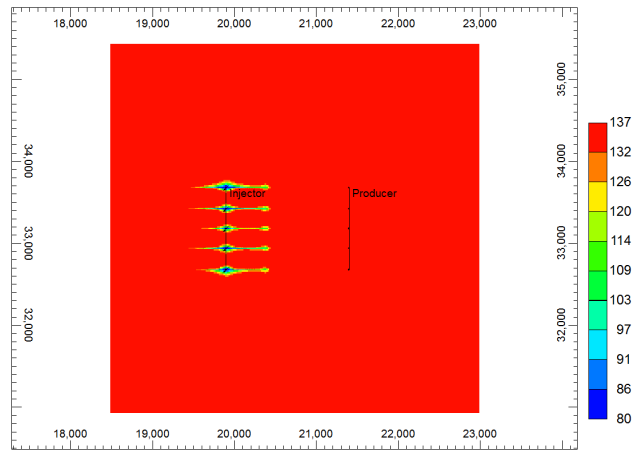


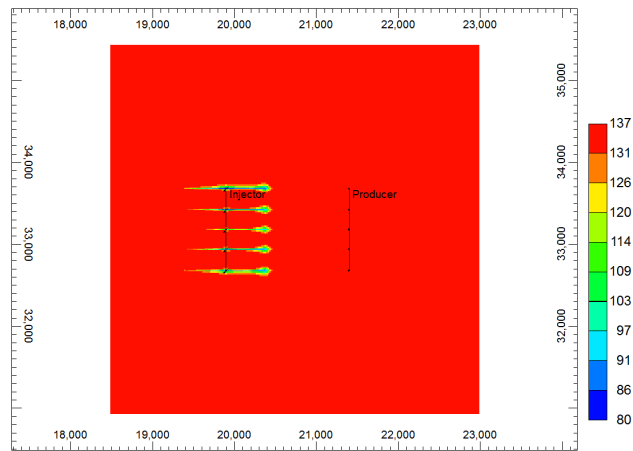
Figure 3.32: Summary of thermal breakthrough time and change of productivity index in the process of time for horizontal well with transverse fracture cases with different dimensionless fracture conductivity values.



(a) $C_{fD} = 1.0$



(b) $C_{fD} = 1.5$



(c) $C_{fD} = 10.0$

Figure 3.33: Aerial view temperature distribution after 1 year of production for horizontal well with transverse fracture cases with different dimensionless fracture conductivity values of 1.0 (a), 1.5 (b) and 10.0 (c).

(Figure 3.33), thus improving the hydraulic behavior and shrinking the thermal breakthrough time. As the fluids arrives at the tip of the fracture faster in (c), the flow is more productive but reaches thermal breakthrough earlier. High dimensionless fracture conductivity is always favorable. However, dimensionless fracture conductivity is constrained by technology, formation condition, and cost. To be conservative a dimensionless fracture conductivity of 1.5 was used for the optimization simulation.

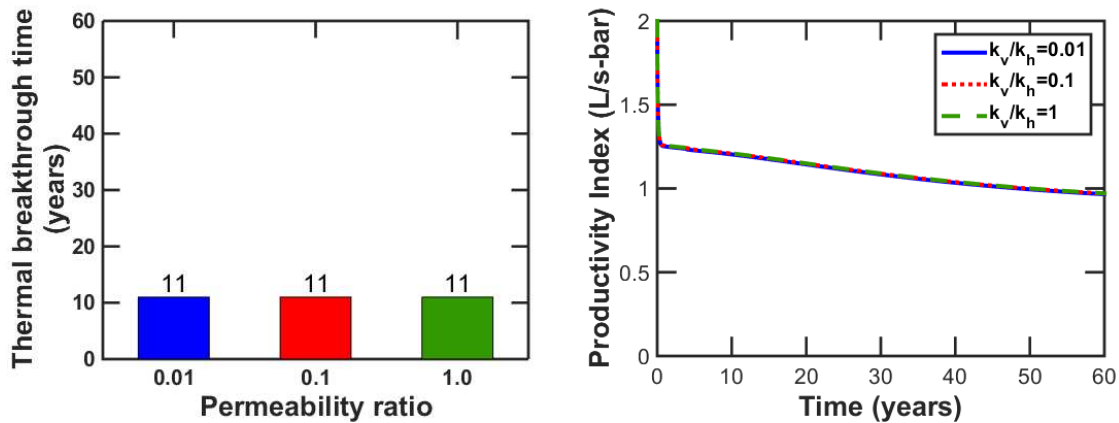


Figure 3.34: Summary of thermal breakthrough time and change of productivity index in the process of time for horizontal well with transverse fracture cases with different ratio of reservoir vertical permeability to horizontal permeability values.

The effect of reservoir permeability ratio (Figure 3.34) performs the same in models A, C, and D where hydraulic fractures are applied in the wells, either vertical wells or horizontal wells. As long as fractures are applied, the fluid flows throughout the entire thickness of the reservoir at the beginning of water injection. Thus, different values of permeability ratio do not affect the flow distribution in the vertical direction. So the thermal evolution and hydraulic behaviors are the same for different permeability ratio values.

In models A and B, none of the cases met the desired flow rate, which indicates that these two models do not improve the hydraulic behavior of the reservoir, so they are not considered for further optimization design. In models C and D, most cases met the desired flow rate, so they are selected for optimization simulation in following sections. The two common variables, that have significant effect of the reservoir simulation results, well spacing and horizontal section length, are determined to be the influential variables for the optimization design. Dimensionless fracture conductivity and

ratio of vertical permeability to horizontal permeability are not selected because they do not have significant impacts on the reservoir behavior. In addition to the studied variables in model C, model D have two more for sensitivity analysis: fracture half-length and fracture spacing. In order to see the effect of these two variables, an extra simulation case, case 19, was run in model D. Case 19 has fracture spacing of 100 m and fracture half-length of 250 m, which shares the same fracture area as in case 2.

Figure 3.35(a) shows that the thermal breakthrough time from case 2 to case 19 increases from 11 years to 21 years. Case 19, which has a shorter fracture half-length, has a longer spacing between the injection and production wells, thus increasing the thermal breakthrough time. Figure 3.35(b) shows that the productivity index decreases about 10 % in the case 19. Because more fractures improve the injection, thus maintaining higher reservoir pressure in case 19, and decreases the productivity index. However, the decrease in productivity index is acceptable, considering the increase in thermal breakthrough time. This hydraulic fracture configuration of 250 m fracture half-length and 100 m fracture spacing was used for optimization simulation in model D.

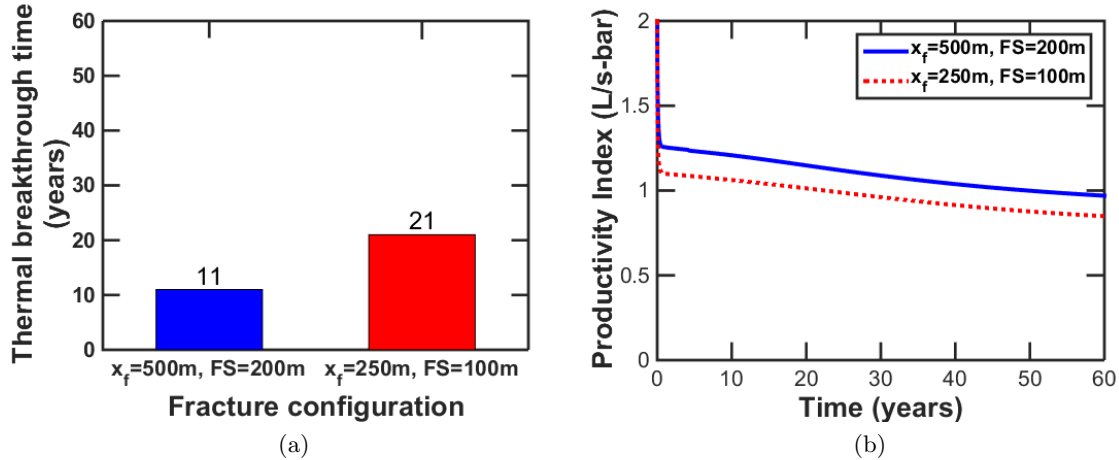


Figure 3.35: Summary of thermal breakthrough and change of productivity index in the process of time horizontal well with transverse fracture cases with same fracture surface area.

3.3 Optimization on horizontal wells with longitudinal hydraulic fractures

The well configuration used consists of two horizontal wells (one injection and one production well) with longitudinal hydraulic fractures (Figure 3.20). The default values applied in this case are

well spacing, D , of 1.5 km and horizontal section length, L , of 1.0 km. The longitudinal hydraulic fractures have a height equal to the total thickness of the reservoir, and length equals to the entire length of the well horizontal section, with a fracture width of 0.1 inch, wellbore radius of 0.086 m, and the dimensionless fracture conductivity of 1.5.

The influential variables considered for the optimization of the geothermal system are the spacing between the injection and production wells, and the length of the horizontal section of the wells. Three values for well spacing were considered: 1.0, 1.2, and 1.5 km, and three values for length of horizontal section: 1.0, 2.0 and 3.0 km. A summary table with the influential variables used in each simulation case is presented in Table 3.6, including thermal breakthrough time, the calculated values for cumulative water production volume at thermal breakthrough time, average productivity index (PI) value from 1 years after injection to thermal breakthrough time, and average flow rate for injection and production wells over 60 years.

Table 3.6: Summary of simulation cases for horizontal wells with longitudinal fractures for calculated performance measures (thermal breakthrough time, cumulative production volume, average productivity index, and average flow rate achieved in injection and production wells)

Simulation case #	1	2	3	4	5	6	7	8	9
Well spacing (km)	1.0	1.0	1.0	1.2	1.2	1.2	1.5	1.5	1.5
Horizontal section length (km)	1.0	2.0	3.0	1.0	2.0	3.0	1.0	2.0	3.0
Thermal breakthrough time (yr)	16	24	29	22	32	38	31	45	52
Cum. prod. vol. ($\times 10^7$ m ³)	2.32	3.48	4.23	3.18	4.64	5.52	4.47	6.51	7.54
Average PI (L/s-bar)	1.21	1.70	1.97	1.08	1.47	1.68	0.93	1.23	1.39
Average flow rate (m ³ /day)	4000	4000	4000	4000	4000	4000	3900*	4000	4000

* indicates average flow rate not meeting desired flow rate because of well restrictions.

The thermal breakthrough time is a function of well configuration and flow rate. Since simulation case 7 did not meet the desired flow rate, the cumulative water production volume at thermal breakthrough time was calculated and used to compare the thermal and hydraulic performance of all simulation cases. The cumulative water production volume is considered to represent the volume of fluid flowing from injection well to production well.

The productivity index is a measure of the hydraulic behavior of the reservoir. It was observed that the injectivity index presents the same trend as the productivity index. For this reason, this work focuses the analysis on the behavior of productivity index exclusively for the discussions

presented in the following sections.

3.3.1 Surface response model for cumulative water produced volume in horizontal wells with longitudinal hydraulic fractures

A stepwise linear regression method is applied to determine a surface response model of cumulative produced water volume, $cumV$, in terms of well spacing, D , and length of horizontal section, L . For the selection of the model terms a backward elimination technique is used, which starts with all terms of the quadratic model showed in Equation 3.2 (constant, linear, interaction and quadratic terms), and then the least significant term is removed (i.e., the one with a p-value greater than a pre-specified significance level of 5%) one by one, until all the remaining terms are statistically significant.

$$cumV = \beta_0 + \beta_1 D + \beta_2 L + \beta_3 DL + \beta_4 D^2 + \beta_5 L^2 \quad (3.2)$$

The coefficients, β_i , are unbiased, have minimum variance, and are estimated using the least squares method. The goodness of fit of the model is quantified by the coefficient of determination, R^2 , and the adjusted coefficient of determination, $adjR^2$. After applying the stepwise linear regression method, the following model is obtained,

$$cumV = \beta_0 + \beta_1 D + \beta_2 L \quad (3.3)$$

The goodness of fit measures for the model in Equation 3.3 are: $R^2 = 0.972$, and $adjR^2 = 0.963$, which are considered acceptable. And the p-value of the constant, D and L are 0.000455, 3.27×10^{-5} and 7.97×10^{-5} , respectively. However this equation is lacking of physical meaning to represent the cumulative water produced volume. The next step was to apply some engineering judgment to define the final terms for the model.

The flow vector distribution after one year of production, calculated using the reservoir simulator, is presented in Figure 3.36. It can be observed that there is radial flow at both ends of the horizontal section, and a tendency of linear flow in between the horizontal laterals of the two wells. The resulting cumulative produced volume is a combination of the linear flow and radial flow regions, and could be represented by the following expressions,

$$cumV_{linear} = DLh \quad (3.4)$$

$$cumV_{rad} = \pi D^2 h \quad (3.5)$$

where $cumV_{linear}$ is the cumulative produced volume due to linear flow between the wells, and $cumV_{rad}$ is the cumulative produced volume due to radial flow at the ends of the horizontal sections, D is well spacing, L is length of horizontal section, and h is the reservoir height.

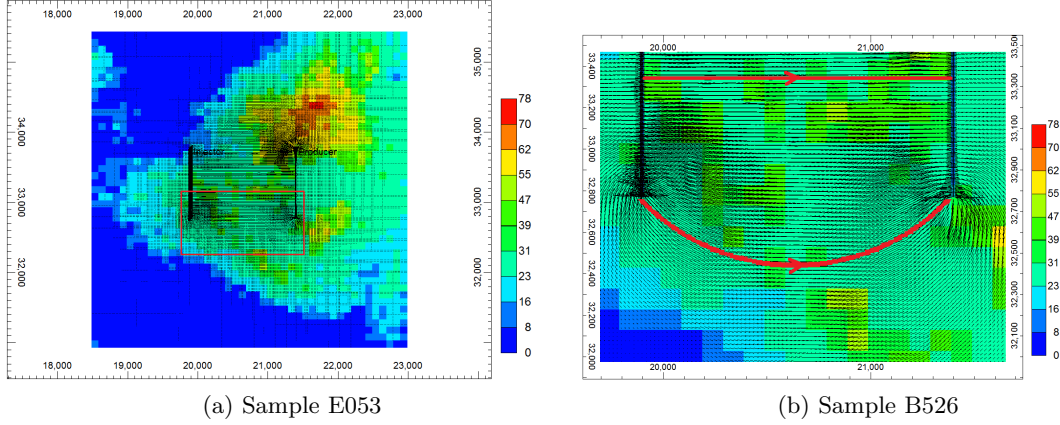


Figure 3.36: Flow vector distribution of horizontal wells with longitudinal fractures after one year of production. Full view on the left and zoomed in view on the right.

Combining Equation 3.4 and Equation 3.5 , the final cumulative water produced volume model should be of the form,

$$cumV = \text{constant} + DLh + \pi D^2 h \quad (3.6)$$

Since h , reservoir height, changes in the reservoir model, the equation is rearranged to include this parameter in a coefficient that averages these changes as follows,

$$cumV = \beta_0 + \beta_1 DL + \beta_2 D^2 \quad (3.7)$$

For this model (Equation 3.7), the p -values of the constant, DL and D^2 terms are 0.750, 7.05×10^{-6} and 6.02×10^{-5} , respectively. The R^2 is 0.998 and $adjR^2$ is 0.984. Since the p -value for the constant term is higher the significance level of 5%, it is removed. The resulting model representing cumulative produced volume in terms of well spacing and horizontal section length is presented in Equation 3.8. For this model, p -values of the DL and D^2 terms are 7.87×10^{-7} and 1.87×10^{-6} . The R^2 is 0.987 and $adjR^2$ is 0.987, confirming the validity of the model and improving upon the previous model (Equation 3.3). A plot of the resulting model for cumulative produced water volume is presented in Figure 3.37, along with the simulation results used to develop the model.

$$cumV = 0.99637DL + 1.4254D^2 \quad (3.8)$$

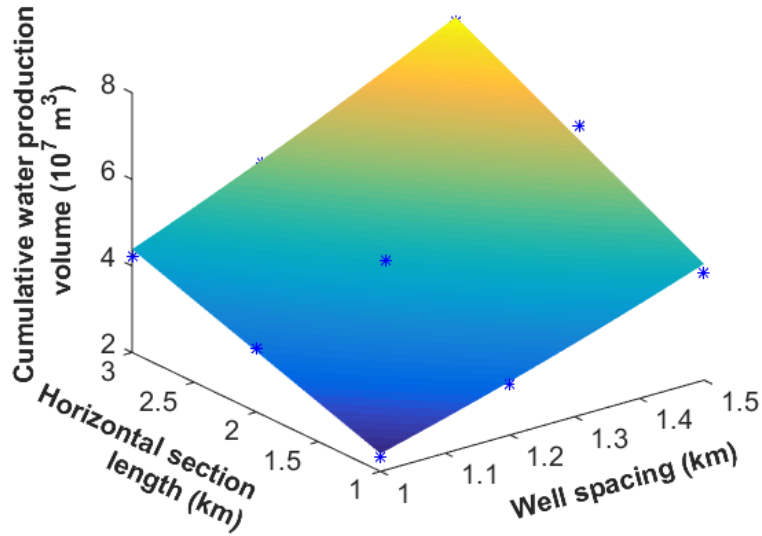


Figure 3.37: 3D plot of cumulative water produced volume as function of horizontal section length and well spacing in horizontal wells with longitudinal fractures. The blue asterisks are the simulation result data points.

3.3.2 Surface response model for productivity index in horizontal wells with longitudinal hydraulic fractures

Productivity Index, PI , expresses the fluid deliverability of a reservoir to the wellbore. It is calculated as the flow rate delivered per pressure drawdown at the sandface. Pressure drawdown is the difference between the average reservoir pressure and the flowing bottomhole pressure in the well. Sandface is the physical interface between the formation and the wellbore. By definition,

$$PI = \frac{Q}{\Delta p} = \frac{Q}{p_{res} - p_{prod}} \quad (3.9)$$

where Q is the production well flow rate, p_{res} is the average reservoir pressure, and p_{prod} is the production well bottomhole pressure.

The Darcy's law for single phase flow in a horizontal porous media can be written as,

$$Q = -\frac{k}{\mu} A \left(\frac{\Delta p}{D} \right) \quad (3.10)$$

where k is the reservoir permeability, μ is the fluid viscosity, A is the cross-sectional area to flow (in this case, the area is the product of reservoir height and length of horizontal section), Δp

is the pressure drop over a given distance of D (in this case, the distance is the well spacing). Substituting the flow rate expression from Darcy's Law (Equation 3.10) into Equation 3.9, the Productivity Index equation in linear flow is,

$$PI_{linear} = \frac{Q}{\Delta p} = -\frac{kh}{\mu} \frac{L}{D} \quad (3.11)$$

where h is the reservoir height, L is the length of the well horizontal section and D is the well spacing between injection well and production well.

The Darcy's law for single phase radial flow can be written as,

$$Q = -\frac{k}{\mu} A \left(\frac{dp}{dr} \right) \quad (3.12)$$

where A is the cross-sectional area to flow, which in this case is the product of the reservoir height and radial flow circumference, $\frac{dp}{dr}$ is the pressure drop from the wellbore to the boundary of the drainage area.

Substituting the flow rate expression from the radial Darcy's law into the Productivity Index equation,

$$PI_{rad} = \frac{Q}{\Delta p} = -\frac{2\pi kh}{\mu} \left[\ln \frac{D}{r_{well}} \right]^{-1} \quad (3.13)$$

where D is the well spacing between injection well and production well and r_{well} is the wellbore radius.

A model that represents the behavior of the PI for the pair of horizontal wells with longitudinal fractures, should combine the linear and radial forms obtained for productivity index as follows,

$$PI = \text{constant} - \frac{kh}{\mu} \frac{L}{D} - \frac{2\pi kh}{\mu} \left[\ln \frac{D}{r_{well}} \right]^{-1} \quad (3.14)$$

A general form for the model of PI in terms of well spacing and horizontal section length is obtained by combining the parameters and properties in Equation 3.14 into more general coefficients,

$$PI = \beta_0 + \beta_1 \left[\ln \frac{D}{r_{well}} \right]^{-1} + \beta_2 \frac{L}{D} \quad (3.15)$$

For this model the p -values of the intercept, $\left[\ln \frac{D}{r_{well}} \right]^{-1}$ and $\frac{L}{D}$ terms are 0.0124, 0.0573 and 8.30×10^{-6} , respectively, which are within the specified significance level. The R^2 is 0.98, and $adjR^2$ is 0.974. The resulting model representing productivity index as function of well spacing and horizontal section length is presented in Equation 3.16. A plot of the resulting model for

productivity index is presented in Figure 3.38, along with the simulation results used to develop the model.

$$PI = -3.9003 + 44.871 \left[\ln \frac{D}{r_{well}} \right]^{-1} + 0.36627 \frac{L}{D} \quad (3.16)$$

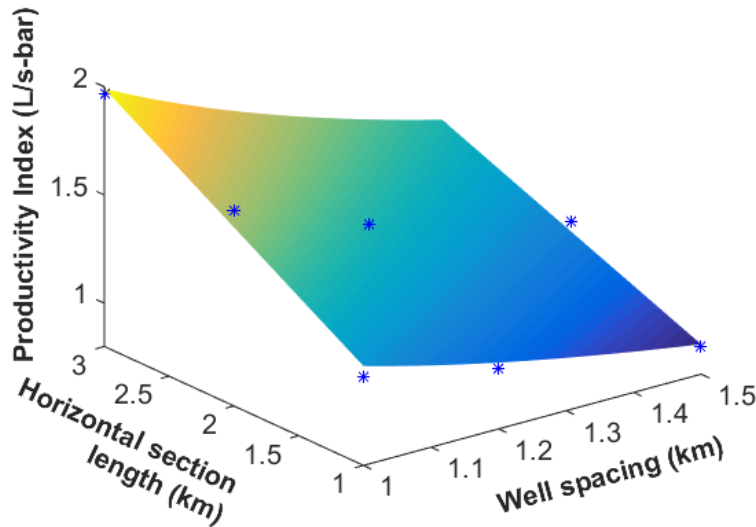


Figure 3.38: 3D plot of PI as function of horizontal section length and well spacing in horizontal wells with longitudinal fractures. The blue asterisks are the simulation result data points.

3.3.3 Optimal well configuration in horizontal wells with longitudinal hydraulic fractures

The response surface models obtained in Section 3.3.1 and Section 3.3.2 are simplified representations of the thermal-hydraulic behavior of the sedimentary geothermal system with two horizontal wells with longitudinal hydraulic fractures. The hydraulic behavior of the reservoir was constrained by imposing restrictions to the well bottomhole pressure values (i.e., a maximum injection pressure and a minimum production pressure). Using the response surface models, it is possible to determine the well configurations (in terms of the influential variables) that achieve a specific thermal breakthrough time of 30 years; the constraint imposed to the thermal behavior of the geothermal system. This constraint can be expressed in terms of the cumulative produced water volume ($cumV_{30years}$) by multiplying the desired flow rate by the desired thermal breakthrough time of 30 years in Equation 3.17. The cases that do not meet the desired flow rate, because of poor hydraulic performance,

will have a larger cumulative produced volume, while the cases that exhibit an earlier breakthrough time will have a lower cumulative produced volume. Figure 3.39 shows the surface response model for the cumulative produced volume as function of well spacing and horizontal section length, and highlights the interception of this model with a constant plane of $cumV_{30years}$. The red curve is the interception between the surface response model for cumulative produced water and the constant plane, and represents the well configuration with a breakthrough time of 30 years and meets the desired flow rate. The portion of the model that is above the constant plane, represents the well configurations with a cumulative production larger that the production volume at the desired flow rate during 30 years. The portion of the model that is below the constant plane, represents the well configurations that produces less than the production of 30 years at the desired flow rate.

$$cumV_{30years} = Q \times time = 4000 \frac{m^3}{day} \times 365.25 \frac{days}{year} \times 30years = 4.38 \times 10^7 m^3 \quad (3.17)$$

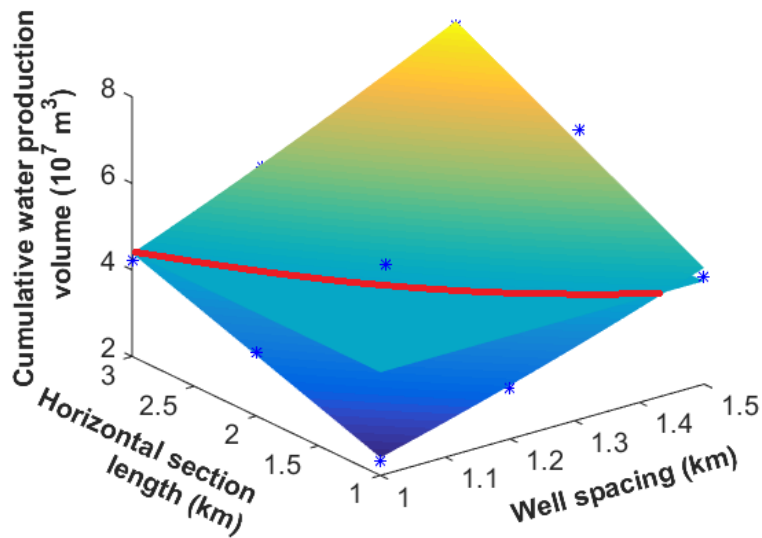


Figure 3.39: Surface interaction of cumulative water production volume at different values of horizontal section length and well spacing and cumulative water production volume at 30 years, in horizontal wells with longitudinal fractures. The blue asterisks are the simulation result data points.

The intersection curve can be represented using the following equation,

$$4.38 = 0.99637DL + 1.4254D^2 \quad (3.18)$$

where L ranges from 1 to 3, and D ranges from 1.0 to 1.4 (calculated at $L=3$ and $L=1$). Solving for L in terms of D ,

$$L = \frac{4.38 - 1.4254D^2}{0.99637D} \quad (3.19)$$

Substituting in the equation for the PI in terms of L and D (Equation 3.16), a PI equation in terms of D along the interception curve is obtained,

$$PI = -3.9003 + 44.871 \left[\ln \frac{D}{r_{well}} \right]^{-1} + 0.36627 \frac{1}{D} \left(\frac{4.38 - 1.4254D^2}{0.99637D} \right) \quad (3.20)$$

Equation 3.20 can be used to calculate the values of PI for the well configuration that have a thermal breakthrough time of 30 years, as shown in Figure 3.40. It can be observed that a minimum well spacing of 1.0 km provides a maximum PI value. With reference to Figure 3.39, the corresponding horizontal section length is 3.0 km. For a well configuration consisting of horizontal wells with longitudinal hydraulic fractures, a longer horizontal section is both favorable for longer thermal breakthrough time and higher productivity index. A farther well spacing gives a longer thermal breakthrough time, but deteriorates the hydraulic behavior by lowering the PI value. A trade off could be obtained by determining the minimum required well spacing that meets a specific commercial thermal breakthrough time (e.g., considering the lifetime of a power plant).

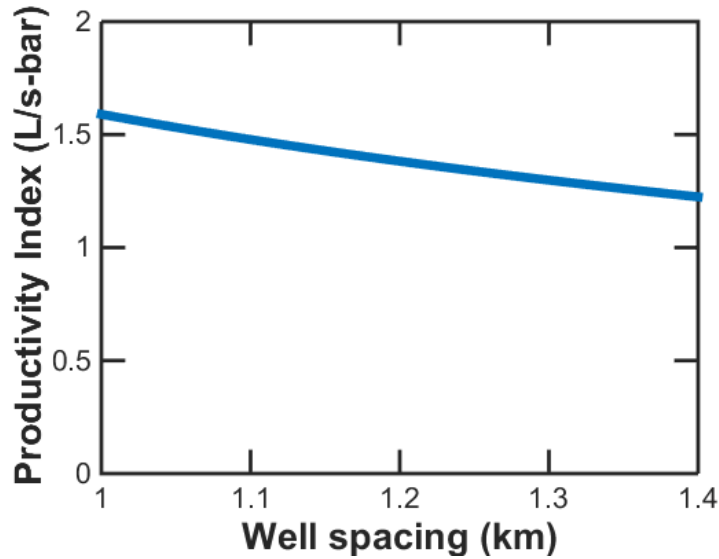


Figure 3.40: Change of PI at different values of well spacing at 30 years of desired flow rate production in horizontal wells with longitudinal fractures.

The optimized case for the Lyons formation sedimentary geothermal system is a doublet horizontal well with longitudinal fractures, with well spacing of 1.0 km and horizontal section length

of 3.0 km, same as case 3.

3.4 Optimization on horizontal wells with multi-stage transverse fractures

As the most efficient well configuration in model D, case D12 was selected for the optimization design in doublet horizontal wells (one injection and one production well) with multi-stage transverse fractures (Figure 3.26). The default values applied in this case are well spacing, D , of 1.5 km, horizontal section length, L , of 1.0 km. The transverse hydraulic fractures have a height equal to the total thickness of the reservoir, half-length equal to 250 m, and fracture spacing of 100 m, with a fracture width of 0.1 inch, wellbore radius of 0.086 m and the dimensionless fracture conductivity of 1.5.

The influential variables considered for the optimization of the geothermal system are the spacing between the injection and production wells, and the length of the horizontal section of the wells. Three values for well spacing were considered: 1.0, 1.5, and 2.0 km, and three values for length of horizontal section: 1.0, 2.0 and 3.0 km. A summary table with the influential variables used in each simulation case is presented in Table 3.7, including thermal breakthrough time, and the calculated values for cumulative production volume at thermal breakthrough time, average productivity index (PI) value after 1 year of production until thermal breakthrough time, and average flow rate for injection and production wells over 60 years.

Table 3.7: Summary of simulation cases for horizontal wells with transverse fractures for calculated performance measures (thermal breakthrough time, cumulative production volume, average productivity index, and average flow rate achieved in injection and production wells)

Simulation case #	1	2	3	4	5	6	7	8	9
Well spacing (km)	1.0	1.0	1.0	1.5	1.5	1.5	2.0	2.0	2.0
Horizontal section length (km)	1.0	2.0	3.0	1.0	2.0	3.0	1.0	2.0	3.0
Thermal breakthrough time (yr)	8	13	18	21	31	39	42	53	60
Cum. prod. vol. ($\times 10^7$ m ³)	1.16	1.90	2.63	3.03	4.50	5.66	5.77	7.66	8.68
Average PI (L/s-bar)	1.32	1.96	2.56	0.98	1.40	1.65	0.79	1.05	1.21
Average flow rate (m ³ /day)	4000	4000	4000	3900*	4000	4000	3700*	4000	4000

* indicates average flow rate not meeting desired flow rate because of well restrictions.

Similar to the analysis in 3.3, since cases 4 and 7 did not meet the desired flow rate, the cumulative water production volume at thermal breakthrough time was calculated and used to

compare the thermal and hydraulic performance of all simulation cases. The cumulative produced volume is considered to represent the volume of fluid flowing from injection well to production well.

3.4.1 Surface response model for cumulative water produced volume in horizontal wells with multi-stage transverse fractures

A stepwise linear regression method is applied to determine a surface response model of cumulative produced water, $cumV$, in terms of well spacing, D , and length of horizontal section, L . For the selection of the model terms a backward elimination technique is used, which starts with all terms of the quadratic model showed in Equation 3.21 (constant, linear, interaction and quadratic terms).

$$cumV = \beta_0 + \beta_1 D + \beta_2 L + \beta_3 DL + \beta_4 D^2 + \beta_5 L^2 \quad (3.21)$$

Step by step, the least significant term is removed when its p -value is greater than a pre-specified significance level of 5%, until all the remaining terms are statistically significant. After applying the stepwise linear regression method, the following model is obtained,

$$cumV = \beta_0 + \beta_1 DL + \beta_2 D^2 \quad (3.22)$$

This equation has the same general form with the cumulative produced volume in horizontal wells with longitudinal fractures in Equation 3.7, confirming the validity of the equation.

Figure 3.41 presents the flow vector distribution after one year of production, calculated using the reservoir simulator. It can be observed that there are radial flows with different radii at both ends of the horizontal section, and a tendency of linear flow in between the horizontal laterals of the two wells. The resulting cumulative produced volume is a combination of the linear flow and radial flow regions, which is verified by the surface response model in Equation 3.22.

For this model (Equation 3.22), the p -values of the constant, DL and D^2 terms are 0.00115, 4.98×10^{-6} , and 7.85×10^{-7} , respectively, which are within the significance level. The R^2 is 0.996, and $adjR^2$ is 0.994, confirming the validity of the model. The resulting model representing cumulative produced water volume in terms of well spacing and horizontal section length is presented in Equation 3.23. A plot of the resulting model for cumulative produced volume is presented in Figure 3.42, along with the simulation results used to develop the model.

$$cumV = -0.92565 + 0.77688DL + 1.3032D^2 \quad (3.23)$$

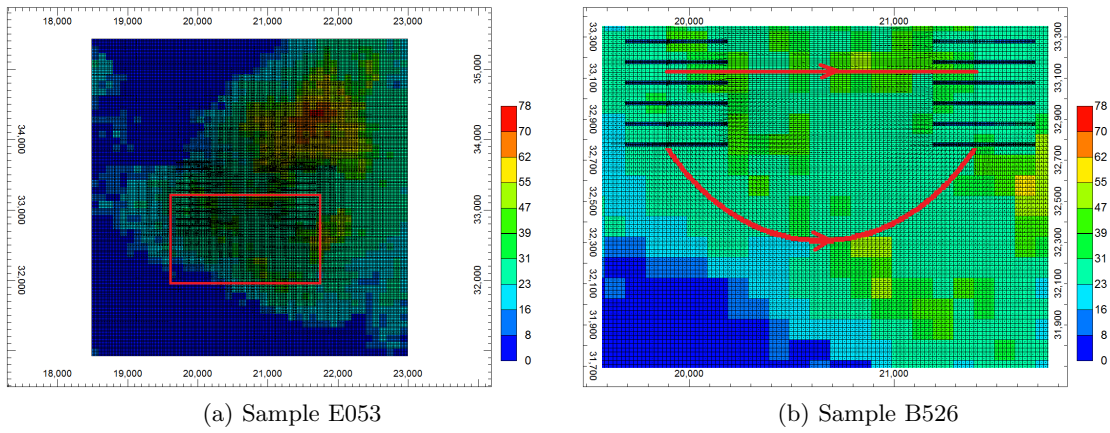


Figure 3.41: Flow vector distribution of horizontal wells with transverse fractures after one year of production. Full view on the left and zoomed in view on the right.

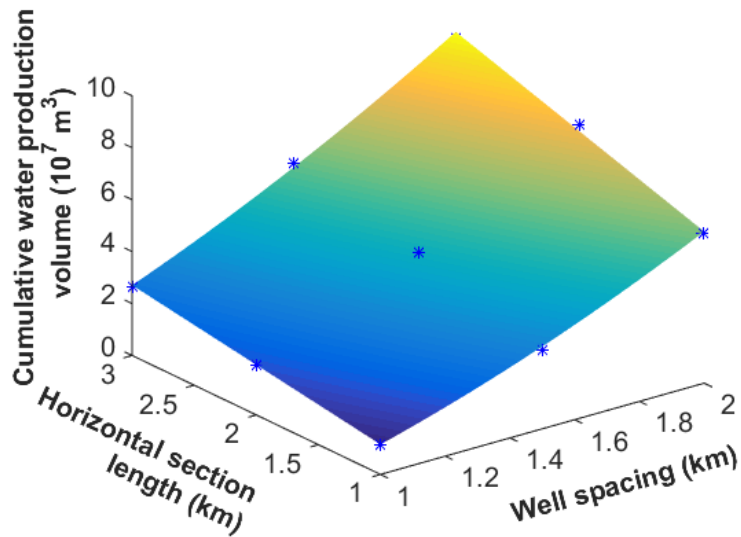


Figure 3.42: 3D plot of cumulative water produced volume as function of horizontal section length and well spacing in horizontal wells with transverse fractures. The blue asterisks are the simulation result data points.

3.4.2 Surface response model for productivity index in horizontal wells with multi-stage transverse fractures

With the same analysis from Section 3.3.2, a general form for the model of PI in terms of well spacing and horizontal section length is shown below,

$$PI = \beta_0 + \beta_1 \left[\ln \frac{D}{r_{well}} \right]^{-1} + \beta_2 \frac{L}{D} \quad (3.24)$$

According to stepwise linear regression method, the surface response model built for this model has the p -values of the intercept, $\left[\ln \frac{D}{r_{well}} \right]^{-1}$ and $\frac{L}{D}$ terms are 0.00212, 0.00129 and 4.66×10^{-6} , respectively, which are within the specified significance level. The R^2 is 0.989, and $adjR^2$ is 0.985. The resulting model representing productivity index as function of well spacing and horizontal section length is presented in Equation 3.25. A plot of the resulting model for productivity index is presented in Figure 3.43, along with the simulation results used to develop the model.

$$PI = -4.5568 + 50.38 \left[\ln \frac{D}{r_{well}} \right]^{-1} + 0.55994 \frac{L}{D} \quad (3.25)$$

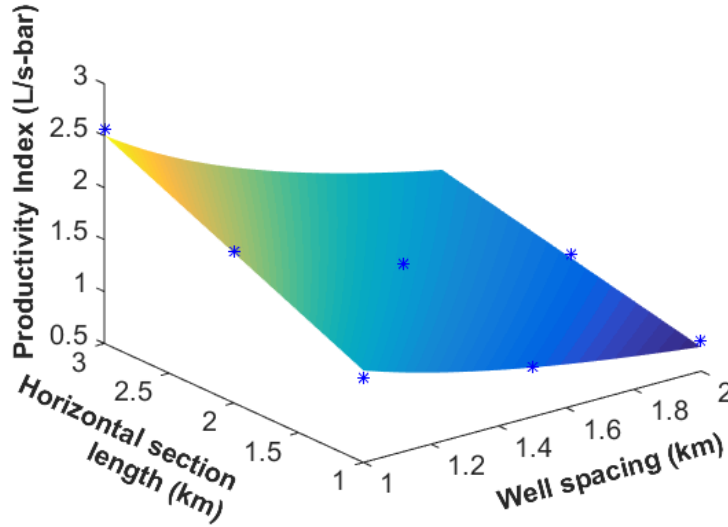


Figure 3.43: 3D plot of PI as function of horizontal section length and well spacing in horizontal wells with transverse fractures. The blue asterisks are the simulation result data points.

3.4.3 Optimal well configuration in horizontal wells with multi-stage transverse fractures

The response surface models obtained in 3.4.1 and 3.4.2 are simplified representations of the thermal-hydraulic behavior of the sedimentary geothermal system with two horizontal wells with transverse hydraulic fractures. Figure 3.44 shows the surface response model for the cumulative produced volume as function of well spacing and horizontal section length, and highlights the interception of this model with a constant plane of $cumV_{30years}$. The red curve is the interception between the surface response model for cumulative produced water and the constant plane, and represents the well configuration with a breakthrough time of 30 years and meets the desired flow rate.

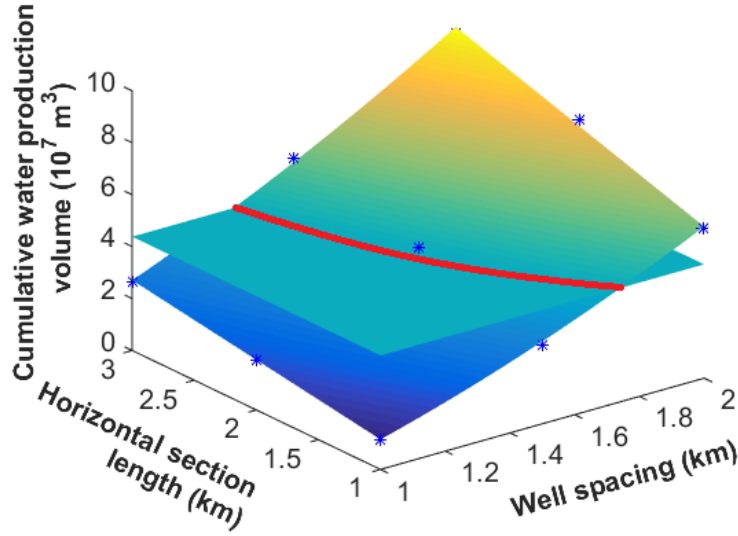


Figure 3.44: Surface interaction of cumulative water production volume at different values of horizontal section length and well spacing and cumulative water production volume at 30 years, in horizontal wells with transverse fractures. The blue asterisks are the simulation result data points.

The intersection curve can be represented using the following equation,

$$4.38 = -0.92565 + 0.77688DL + 1.3032D^2 \quad (3.26)$$

where L ranges from 1 to 3, and D ranges from 1.3 to 1.7 (calculated at $L=3$ and $L=1$). Solving for L in terms of D ,

$$L = \frac{4.38 + 0.92565 - 1.3032D^2}{0.77688D} \quad (3.27)$$

Substituting in the equation for the PI in terms of L and D (Equation 3.25), a Productivity Index equation in terms of D along the interception curve is obtained,

$$PI = -4.5568 + 50.38 \left[\ln \frac{D}{r_{well}} \right]^{-1} + 0.55994 \frac{1}{D} \left(\frac{4.38 + 0.92565 - 1.3032D^2}{0.77688D} \right) \quad (3.28)$$

Equation 3.28 can be used to calculate the values of PI for the well configuration that have a thermal breakthrough time of 30 years, as shown in Figure 3.45. It can be observed that a minimum well spacing of 1.3 km provides a maximum PI value. With reference to Figure 3.44, the corresponding horizontal section length is 3.0 km. For a well configuration consisting of horizontal wells with longitudinal hydraulic fractures, a longer horizontal section is both favorable for longer thermal breakthrough time and higher productivity index. A farther well spacing gives a longer thermal breakthrough time, but deteriorates the hydraulic behavior by lowering the PI value. A trade off could be obtained by determining the minimum required well spacing that meets a specific commercial thermal breakthrough time (e.g., considering the lifetime of a power plant).

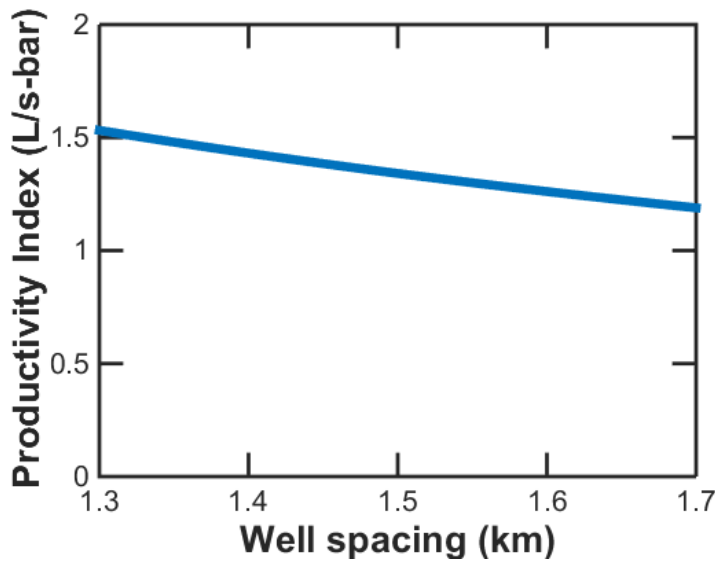


Figure 3.45: Change of PI at different values of well spacing at 30 years of desired flow rate production in horizontal wells with transverse fractures.

The optimized case for the Lyons formation sedimentary geothermal system is a doublet horizontal well with transverse fractures, with well spacing of 1.3 km and horizontal section length of 3.0 km.

3.5 Summary

This chapter presented an overview of the significance of different variables in the design of hydraulic fractures in a geothermal reservoir. An estimation of the permeability in the reservoir is the key component to decide if well enhancement techniques are necessary or not. For a reservoir with too low permeability, if a desired flow rate cannot be reached, more advanced enhancement techniques are required. For a reservoir with high enough permeability, the application of hydraulic fracturing does not improve significantly, so not economical for the production.

A reservoir with intermediate permeability (ranges from 7.81 md to 78 md in this thesis work) is a proper candidate to apply hydraulic fracturing to. Usually, vertical wells with or without fractures, and horizontal wells with open-hole completion cannot provide desired flow rate, which makes them not profitable. Horizontal wells with fractures are advantageous for the flow behavior and thermal evolution. In limited space, a horizontal well doublet system with a long lateral section and short well spacing is preferred for both longitudinal and transverse fracture cases. In addition, in the cases of transverse fractures, shorter fracture spacing contributes more fractures, thus facilitating the flow behavior. In a certain area of interest, both horizontal wells with longitudinal fractures and horizontal wells with transverse fractures facilitate the thermal recovery in a geothermal reservoir. While the former improves more on thermal breakthrough time, and the latter enhances more on the hydraulic behavior.

CHAPTER 4

CONCLUSIONS AND SUGGESTIONS

This thesis represents the necessity and advantage of the application of well enhancement techniques (i.e., hydraulic fracturing) to the production in a sedimentary geothermal reservoir. The objective is to select the optimal well configurations, which maximizes the productivity index and injectivity index, subject to a constraint of minimum thermal breakthrough time in a sedimentary geothermal reservoir. To achieve the goal, eight variables of interest are selected, which would affect the thermal evolution and hydraulic behavior of the geothermal reservoir. Sensitivity of these variables are analyzed in four different well configurations to determine the efficient well configurations and corresponding influential variables. Horizontal wells with longitudinal or transverse fractures are selected because of their improvement on flow behavior and thermal evolution.

4.1 Conclusions

The main conclusions that can be drawn from the research conducted for this thesis are:

1. Permeability acts as the key property in the production of a sedimentary geothermal reservoir. In this research work, the low permeability model has permeability ranges from 2.81 md to 25.2 md. The intermediate permeability model has a permeability range from 7.81 md to 78 md, and the high permeability model has permeability values ranging from 30.3 md to 299 md. Well enhancement techniques may not be sufficient to make a commercial geothermal electricity generation project in a low permeability reservoir. Reservoirs with high enough permeability may not need the optimization process of well configuration in order to meet the desired flow rate for electricity generation. A geothermal reservoir with an intermediate permeability distribution could be a good candidate formation to apply hydraulic fracturing techniques and optimization of well configurations.
2. Hydraulic fracturing techniques improve the production in both vertical wells and horizontal wells. Horizontal wells with fractures have a more beneficial performance compared to vertical wells with fractures. Thus horizontal wells with longitudinal fractures or multi-stage transverse fractures provide good improvement on production.

3. Horizontal wells with longitudinal fractures require long horizontal section length and a minimum well spacing to reach the commercial geothermal reservoir life time and keep a high value of productivity and injectivity.
4. Horizontal wells with transverse fractures with short fracture spacing, long horizontal section length and a minimum well spacing are preferred.
5. In cases with the same swept area, horizontal wells with longitudinal fractures are more favorable in the aspect of thermal breakthrough time, while horizontal wells with transverse fractures are more beneficial in the flow behavior.

4.2 Suggestions

There are some suggestions for future work.

In the sensitivity analysis part, reservoir heterogeneity could affect the simulation result. When considering different values of well horizontal section lengths, fracture half-lengths, and fracture spacing, the change of reservoir behavior could be caused by the variable change or the reservoir heterogeneity. It would be more accurate if reservoir heterogeneity can be taken into consideration.

The geomechanics stress field was not investigated in this research work. If that can be taken into consideration, the well configuration can be further improved by making the fracture direction parallel to the maximum principle stress direction.

In the preliminary simulation, it can be seen that the reservoir permeability determines the maximum reachable value of desired injection and production flow rate, and the flow rate directly affect the thermal breakthrough time. If the relationship between the permeability estimation and the desired flow rate can be determined, the general work flow in optimizing the well configuration process can be applied to different reservoirs, under different production rate needs, more efficiently.

REFERENCES CITED

- Allis, R., Moore, J., Blackett, B., Gwynn, M., Kirby, S., Sprinkel, D., 2011. The potential for basin-centered geothermal resources in the Great Basin. *Geothermal Resources Council Transactions*, 35:683–688.
- Augustine, C., 2014. Analysis of sedimentary geothermal systems using an analytical reservoir model. *Geothermal Resources Council Transactions*, 38:641–647.
- Blodgett, L., Slack, K., 2003. *Geothermal 101: Basics of Geothermal Energy Production and Use*. Technical Report. Geothermal Energy Association. 209 Pennsylvania Avenue SE, Washington, D.C. 20003.
- California Energy Commission, 2015a. California geothermal energy statistics and data. *Quarterly Fuel and Energy Report (QFER)*.
- California Energy Commission, 2015b. QFER CEC-1304 Power Plant Data Reporting. *Quarterly Fuel and Energy Report (QFER)*.
- Cho, J., Augustine, C., Zerpa, L., 2015. Validation of a numerical reservoir model of sedimentary geothermal systems using analytical models. *Stanford Geothermal Workshop*.
- Chrysoberyl, D., 2011. The Denver Basin...(Video). (<http://shaleoilandgas.blogspot.com/2011/04/denver-basinvideo-blog.html>, accessed: 05/04/2015).
- CMG, 2011. *2-day Geostatistics Tutorial*. Computer Modelling Group Ltd.
- Cressie, N., 1993. *Statistics for spatial data*. Wiley Interscience.
- Energy and Geosciences Institute, 1997. *Briefing on Geothermal Energy*. Technical Report. U.S. Geothermal Industry for the Renewable Energy Task Force. Washington, D.C.
- Geothermal Technologies Office, 2012. *Geothermal Electricity Technology Evaluation Model (GETEM)*. U.S. Department of Energy.
- Gringarten, A.C., Sauty, J.P., 1975. A theoretical study of heat extraction from aquifers with uniform regional flow. *Journal of Geophysical Research*, 80(35):4956–4962.
- Hershey, L.A., Schneider, P.A.J., 1964. Ground-water investigations in the lower Cache la Poudre River Basin, Colorado. *Geological Survey Water-Supply Paper*, 1669(X).

- Higley, D.K., Cox, D.O., 2007. *Petroleum Systems and Assessment of Undiscovered Oil and Gas in the Denver Basin Province, Colorado, Kansas, Nebraska, South Dakota, and Wyoming* USGS Province 39. U.S. Geological Survey Digital Data Series DDS69P. chapter Oil and Gas Exploration and Development along the Front Range in the Denver Basin of Colorado, Nebraska, and Wyoming.
- Kirby, S.M., 2012. Summary of compiled permeability with depth measurements for basin fill, igneous, carbonate, and siliciclastic rocks in the Great Basin and adjoining regions. *Utah Department of Natural Resources*.
- Lopez, S., Hamm, V., Brun, M., Schaper, L., Boissier, F., Cotiche, C., Giuglaris, E., 2010. 40 years of Dogger aquifer management in Ile-de-France, Paris Basin, France. *Geothermics*, 39:339–356.
- Matheron, G., 1963. Principles of geostatistics. *Economic Geology*, 58:1246–1266.
- Menjzo, A., Sauty, J., 1982. Characteristics and effects of geothermal resources exploitation. *Journal of Hydrology*, 56(1):49 – 59.
- Meyer, H., McGee, H., 1985. Oil and gas fields accompanied by geothermal anomalies in Rocky Mountain region. *AAPG Bulletin*, 69(6):933–945.
- Milito, S., 2010. Permian Lyons sandstone 280 mya. (<http://www.paleotrailsproject.org/index.html>, accessed: 08/19/2014).
- Moeck, I.S., 2014. Catalog of geothermal play types based on geologic controls. *Renewable and Sustainable Energy Reviews*, 37:867–882.
- NREL, 2010. Geothermal prospector. (<https://maps.nrel.gov/geothermal-prospector/>, accessed: 02/12/2016).
- Pearson, C.M., 2001. Dimensionless fracture conductivity: Better input values make better wells. *Journal of Petroleum Technology*, 53(01):59–63.
- Sanjuan, B., Laplaige, P., 2013. *France Country Report*. Technical Report. IEA Geothermal Implementing Agreement.
- Sass, J., Priest, S., 2002. Geothermal California. *GRC Bulletin*, pp. 183–187.
- Schellschmidt, R., Sanner, B., Pester, S., Schulz, R., 2010. Geothermal energy use in germany. *Proceedings World Geothermal Congress*, (0152):19.
- Szanyi, J., Kovcs, B., 2010. Utilization of geothermal systems in south-east Hungary. *Geothermics*, 39:357–365.
- Szanyi, J., Kovcs, B., Scharek, E.P., 2009. Geothermal energy in Hungary: potentials and barriers. *European Geologist*, (27):15–18.

Verly, G., 1993. *Generation, Accumulation and Production of Europe's Hydrocarbons III: Special Publication of the European Association of Petroleum Geoscientists No. 3*. Springer Berlin Heidelberg, Berlin, Heidelberg. chapter Sequential Gaussian Simulation: A Monte Carlo Method for Generating Models of Porosity and Permeability. pp. 345–356.

APPENDIX A - RESERVOIR PROPERTIES

As shown below, Table A.1, Table A.2, Table A.3 and Table A.4 are the common fluid properties, rock properties, reservoir properties and well properties for models A, B, C and D.

Table A.1: Common grid system and reservoir properties of the doublet system

Parameter	Value
Grid type	Orthogonal Corner Point
Grid resolution (m)	20×20×3.58
Reservoir dimensions (m)	4500×4500×35.8
Number of grids before refinement	506250
Simulated fracture width (m)	0.152
Maximum porosity (fraction)	0.191
Mode porosity (fraction)	0.172
Permeability I (mD)	Correlation of porosity
Permeability J (mD)	=PermI
Permeability K (mD)	=PermI×0.1
Reservoir depth (m)	2489-2789
Initial reservoir temperature (°C)	137
Total volumetric heat capacity of reservoir (kJ/m ³ -°C)	2975.23

Table A.2: Common fluid properties of the doublet system

Input parameter	Value
Water specific heat capacity (kJ/kg-°C)	4.27
Water volumetric heat capacity (kJ/m ³ -°C)	3966.83
Liquid phase water heat capacity (J/gmol-°C)	76.95
Water compressibility (1/kPa)	0
Water thermal conductivity (J/m-day-°C)	53500

Table A.3: Common rock properties of the doublet system

Input parameter	Value
Rock density (kg/m^3)	2650
Rock fracture gradient (psi/ft)	0.6
Rock specific heat capacity ($\text{kJ}/\text{kg}\cdot^\circ\text{C}$)	1.045
Rock volumetric heat capacity ($\text{kJ}/\text{m}^3\cdot^\circ\text{C}$)	2380
Rock compressibility ($1/\text{kPa}$)	4.35×10^{-7}
Rock thermal conductivity ($\text{J}/\text{m}\cdot\text{day}\cdot^\circ\text{C}$)	1.496×10^5
Overburden/Underburden heat loss ($\text{kJ}/\text{m}^3\cdot^\circ\text{C}$)	0

Table A.4: Common well properties of the doublet system

Input parameter	Value
Injection rate (m^3/day)	4000
Production rate (m^3/day)	4000
Injection water temperature ($^\circ\text{C}$)	80
Maximum injection well bottomhole pressure (kPa)	35269
Minimum production well bottomhole pressure (kPa)	21348
Wellbore radius (m)	0.086

APPENDIX B - SIMULATION PROPERTIES CALCULATION

In a production well, hot water flows up spontaneously with the pressure from the bottomhole. As fluid flows up, friction loss from the pipeline and loss from hydrostatic pressure might cause the water flash into steam. To prevent that, a lineshaft pump will be set to its deepest possible location, to shorten the distance the water needs to flow up spontaneously. The minimum production well bottomhole pressure is calculated as follows, Main equation: Bernoullis equation (incompressible fluid) in terms of energy head

$$\frac{p_1}{\gamma_w} + \frac{v_1^2}{2g} + z_1 = \frac{p_2}{\gamma_w} + \frac{v_2^2}{2g} + z_2 + h_{f2} \quad (\text{B.1})$$

expanding into detailed terms,

$$\frac{p_1}{\rho_w g} + \frac{v_1^2}{2g} + z_1 = \frac{p_2}{\rho_w g} + \frac{v_2^2}{2g} + z_2 + f \frac{z_2 - z_1}{D} \frac{v_2^2}{2g} \quad (\text{B.2})$$

Point 1 is at the bottomhole and point 2 is at the pump location. In order to avoid water flashing, the minimum required pressure at the pump location, p_2 , is selected as the boiling pressure under water temperature of 137 °C. From National Institute of Standards and Technology Chemistry Webbook, the boiling pressure is 0.332 MPa, and the density of water, ρ_w , is 929 kg/m³, viscosity of water, μ_{w} is 0.0002 Pa·s. A safety margin of 50 psig for the pump is added to the pressure at point 1 as it is the default value used in the GEOTHERMAL ELECTRICITY TECHNOLOGY EVALUATION MODEL (GETEM) (Geothermal Technologies Office 2012). The pressure at point 2, p_2 , equals 675,417 kPa.

The bottomhole depth is selected to be the deepest the location among all 12 water disposal wells to insure the required bottomhole pressure is a minimum value; and the value is 296 ft (2833.4 m). The pump depth is 2000 ft (609.6 m). In the calculation of Bernoulli equation, the depths are transferred into elevation. Elevation at the bottomhole (point 1), z_1 , is zero. Elevation at the pump location (point 2), z_2 , is 2223.8 m. The pipe roughness is 0.1 mm and the friction factor, f , is read to be 0.017 from Moody diagram. p_1 is calculated to be 21,348 kPa, and it is assigned to the minimum production well bottomhole pressure, $BHP_{prod,min}$.

The maximum injector bottomhole pressure ($BHP_{prod,min}$) is the pressure the injector wellbore can bear without fracturing the reservoir formation. Fracture gradient for Lyons Formation sandstone is 0.6 psi/ft.

The maximum injection well bottomhole pressure is calculated to be 35,269 kPa in Equation B.3:

$$BHP_{inj,max} = FG \times D_{reservoirtop} \quad (B.3)$$

A calculation of default dimensionless fracture conductivity is shown below. The default fracture half-length, x_f , is 500 m. Real dimensionless fracture conductivity is chosen to be 1.5. w_{real} is the typical value in hydraulic fracture width, 0.1 in, equaling to 0.00254 m. The mode value of the reservoir permeability, 7.81md, is used for simulation fracture permeability calculation. According to Equation 1.7, $k_{f,real}$ has a value of 2,306,102 mD. w_{sim} is chosen to be 0.152 m for the simulator, so $k_{f,sim}$ is calculated to be 38,536 mD, rounding to nearest 1,000 to be 39,000 mD for the default case.

Thermal breakthrough time is calculated in the Equation B.4 (Gringarten and Sauty 1975):

$$\Delta t = [\phi + (1 - \phi)] \frac{\rho_r C_r}{\rho_w C_w} \frac{\pi D^2 h}{3 Q} \quad (B.4)$$

Where D is the distance between wells in meters, Q is the volumetric injection/production well flow rate in the unit of m³/day, h is reservoir thickness in meters, ϕ is the mode reservoir porosity value, $\rho_w C_w$ is the water heat capacity in kJ/m³-°C and $\rho_r C_r$ is the rock heat capacity in kJ/m³-°C.

APPENDIX C - CORE MEASUREMENTS DATA

Table C.1: Core measurement data for sample E053

Sample depth (ft)	Porosity (fraction)	Permeability (md)
9174.5	0.167	155.0
9175.5	0.162	125.0
9176.5	0.120	14.0
9177.5	0.119	-
9178.5	0.089	0.9
9179.5	0.082	-
9180.5	0.054	1.4
9181.5	0.069	1.3
9182.5	0.142	29.0
9183.5	0.133	7.5
9184.5	0.101	5.7
9185.5	0.041	2.1
9186.5	0.050	-
9187.5	0.032	1.6
9188.5	0.039	1.3
9189.5	0.048	0.0
9190.5	0.059	0.0
9191.5	0.057	0.0
9192.5	0.063	0.0
9193.5	0.054	0.0
9194.5	0.066	3.8
9195.5	0.057	1.1
9196.5	0.093	0.0
9197.5	0.096	0.0
9198.5	0.133	2.1
9199.5	0.149	4.1
9200.5	0.132	1.7
9201.5	0.115	2.2
9202.5	0.126	0.0
9203.5	0.158	3.1
9204.5	0.138	35.0
9205.5	0.184	159.0
9206.5	0.188	156.0
9207.5	0.132	3.5
9208.5	0.125	2.9
9209.5	0.158	2.2
9210.5	0.084	3.2
9211.5	0.147	1.4
9212.5	0.109	-

Table C.1: Continued.

Sample depth (ft)	Porosity (fraction)	Permeability (md)
9213.5	0.110	0.0
9214.5	0.111	0.0
9215.5	0.094	1.9
9216.5	0.115	1.8
9217.5	0.148	1.9
9218.5	0.097	1.7
9219.5	0.125	1.6
9220.5	0.117	3.0
9221.5	0.062	0.0
9222.5	0.087	0.8
9223.5	0.072	-
9224.5	0.039	-
9225.5	0.063	0.0
9226.5	0.030	1.3
9227.5	0.060	0.0
9228.5	0.073	0.0
9229.5	0.063	0.0
9231.5	0.085	0.0
9232.5	0.033	0.0
9233.5	0.066	0.0

Table C.2: Core measurement data for sample B526

Sample depth (ft)	Porosity (fraction)	Permeability (mD)
9026.10	0.0964	8.91
9040.40	0.1713	116.
9046.00	0.0824	0.991
9056.20	0.1399	7.60
9060.80	0.1445	3.93
9062.30	0.1195	1.42
9069.00	0.093	1.03

Table C.3: Core measurement data for sample D485

Sample depth (ft)	Porosity (fraction)	Permeability (md)
6123.0	0.082	-
6124.0	0.180	695.0
6125.0	0.143	1400.0
6126.0	0.188	-
6127.0	0.173	975.0
6128.0	0.124	29.0
6129.0	0.086	0.4
6130.0	0.087	1.0
6131.0	0.069	0.7
6132.0	0.043	2.3
6133.0	0.125	4.1
6134.0	0.049	0.4
6135.0	0.079	0.5
6136.0	0.148	7.9
6137.0	0.159	97.0
6138.0	0.165	404.0
6139.0	0.164	760.0
6140.0	0.089	352.0
6141.0	0.132	83.0
6142.0	0.145	18.0
6143.0	0.084	25.0
6144.0	0.102	293.0
6145.0	0.139	35.0
6146.0	0.103	110.0
6147.0	0.140	32.0
6148.0	0.091	221.0
6149.0	0.064	13.0
6150.0	0.053	3.3
6151.0	0.110	16.0
6152.0	0.116	7.4
6153.0	0.107	61.0
6154.0	0.126	26.0
6155.0	0.089	15.0
6156.0	0.132	14.0
6157.0	0.137	51.0
6158.0	0.199	5.4
6159.0	0.196	630.0
6160.0	0.106	16.0
6161.0	0.143	142.0
6162.0	0.127	0.9
6163.0	0.043	-